Coverage Analysis of Reconfigurable Intelligent Surface Assisted THz Wireless Systems

ALEXANDROS-APOSTOLOS A. BOULOGEORGOS (Senior Member, IEEE),
AND ANGELIKI ALEXIOU (Member, IEEE)

Department of Digital Systems, University of Piraeus, 18534 Piraeus, Greece

CORRESPONDING AUTHOR: ALEXANDROS-APOSTOLOS A. BOULOGEORGOS (e-mail: al.boulogeorgos@ieee.org)

ABSTRACT This paper presents a connectivity analysis of reconfigurable intelligent surface (RIS) assisted terahertz (THz) wireless systems. Specifically, a system model that accommodates the particularities of THz band links as well as the characteristics of the RIS is reported, accompanied by a novel general end-to-end (e2e) channel attenuation formula. Based on this formula, we derive a closed-form expression that returns the optimal phase shifting of each reflection unit (RU) of the RIS. Moreover, we provide a tractable e2e channel coefficient approximation that is suitable for analyzing the RIS-assisted THz wireless system performance. Building upon the aforementioned approximation as well as the assumption that the user equipments are located in random positions within a circular cluster, we present the theoretical framework that quantifies the coverage performance of the system under investigation. In more detail, we deliver a novel closed-form expression for the coverage probability that reveals that there exists a minimum transmission power that guarantees 100% coverage probability. Both the derived channel model as well as the coverage probability are validated through extensive simulations and reveal the importance of taking into account both the THz channel particularities and the RIS characteristics, when assessing the system's performance and designing RIS-assisted THz wireless systems.

INDEX TERMS Channel modeling, connectivity analysis, coverage probability, reconfigurable intelligent surfaces, terahertz wireless systems.

NOMENCLATURE

3D	Three Dimensional
6G	Sixth Generation
AF	Amplify-and-Forward
AHBF	Azimuth Half-Power Beamwidth
AP	Access Point
CDF	Cumulative Distribution Function
e2e	End-to-End
EHPB	Elevation Half-Power Beamwidth
HITRAN	HIgh Resolution TRansmission AbsorptioN
ITU	International Telecommunication Union
LoS	Line-of-Sight
PDF	Probability Density Function
PL	Path-Loss
RIS	Reconfigurable Intelligent Surface
RU	Reflection Unit
RX	Receiver
SNR	Signal-to-Noise-Ratio
THz	Terahertz
TX	Transmitter
UE	User Equipment

I. INTRODUCTION

According to the international telecommunication union (ITU), the global mobile traffic is expected to continue its exponential growth, reaching 5 zettabytes per month by 2020 [1]. This increase is driven by emerging data rate hungry applications, like virtual, augmented and extended reality, virtual presence by means of holographic projection, autonomous vehicles, and others [2]–[4]. Looking forward to

the sixth generation (6 G) era, two main approaches have been identified as candidate technology enabler to support these unprecedented traffic demands [5], [6]. The first one is to exploit higher-frequency bands, with emphasis to the terahertz (THz) [7]–[14], while the second one lies to the use of reconfigurable intelligent surfaces (RISs) capable of alternating their electromagentic properties and thus devising a beneficial wireless propagation environment [15]–[20].

Scanning the technical literature, we can observe a fast growing research effort on analyzing, optimizing, designing, developing and demonstrating wireless THz systems [21]–[38]. In more detail, in [21] and [22], Jornet et. al used radiative transfer theory to extract a propagation model for nano-scale THz communications, while, in [23], Yang et. al presented a channel model for body-centric THz nano-scale networks. Moreover, in [25], the authors reported a simplified path-loss (PL) model for the 275–400GHz band. This work was extended in [26], in order to include the impact of secondary reflections, and it was used as a basic propagation model for several works that analyze the wireless THz system performance, such as [27]–[30], and propose physical and/or medium access control strategies, like [31]–[33]. Meanwhile, in [34], the authors introduced a PL model for nano-sensor THz networks for plant foliage applications, while, in [35], a propagation model for intra-body nano-scale communications was proposed. Moreover, in [36], the authors presented a multi-ray THz propagation model. Likewise, in [37], the authors revealed and quantified the detrimental effect of blockage in THz wireless systems, whereas, in [38], the authors presented a testbed for THz communications in the 275 to 325 GHz. Additionally, in [39], the impact of human blockage in low-THz wireless systems was discussed. Similarly, in [40], the authors performed coverage analysis in THz wireless systems that experience blockage. Finally, in [41], the authors evaluated the effect of blockage in the association process in THz wireless systems.

All the aforementioned contributions agree that line-of-sight (LoS) channel attenuation and blockage are the main limiting factors of THz wireless systems. To break the barriers set by blockage, recently, some research works proposed the use of RIS [6], [16]–[19], [42]–[47]. In particular, in [6], [18], and [19], the authors explained how RIS can be used to mitigate the impact of blockage and introduced the idea of reflected LoS links. In this direction, in [42], the authors conducted an asymptotic uplink ergodic capacity study, assuming that the transmitter (TX)-RIS and RIS-receiver (RX) channels follow Rician distribution, whereas, in [16] and [17], the optimization framework for the maximization of the RX received power was presented. Similarly, in [43] the joint maximization of the sum-rate and energy efficiency was studied for a multi-user downlink scenario, in which connectivity was established by means of reflected LoS. Additionally, in [44], an error analysis was performed for RIS-assisted non-orthogonal multiple access networks. Moreover, in [45], di Renzo et. al highlighted the fundamental similarities and differences between RISs and relays. In the same direction, in [46], the

authors compared the performance of RIS-assisted systems against decode-and-forward relaying ones in terms of energy efficiency, while, in [47], the authors conducted a performance comparison between RIS and amplify-and-forward (AF) relays in terms of average received signal-to-noise-ratio (SNR), outage probability, diversity order and gain, symbol error rate and ergodic capacity, which revealed that, in general, RIS-assisted wireless systems can outperform the corresponding AF relaying ones. Finally, in [48], the impact of hardware imperfections in RIS-assisted wireless systems was quantified in terms of outage probability and diversity order.

To the best of the authors knowledge, there are only a few published works that examine the use of RIS in THz wireless systems [49]–[52]. In [49] and [50], although the directional nature of the THz links was taken into account, the PL characteristics of the transmission path were neglected, while, in [52], the design characteristics of the RIS as well as its functionality were not taken into account. Finally, in [51], the impact of molecular absorption loss was ignored, despite of its paramount importance in the THz band, which was highlighted in several previous contributions (see e.g., [27], [33], [53], [54] and reference therein). The main reason behind this is the lack of tractable channel model for RIS-assisted systems operating in the THz band that accommodates both the building blocks of such systems and the particularities of the THz band. In more detail, this model should take into account the transceivers' antenna gains as well as their position in respect to the RIS position, the transmission frequency, the characteristics of the reflection units (RUS), namely number and dimensions of reflection elements, reflection coefficients, antenna patterns and phase shifts of each one of the RU, as well as the environmental conditions, while being tractable in order to become a useful tool for analyzing the performance of such systems. Motivated by this, this paper focuses on covering this gap by providing a low-complexity channel model that takes into account the particularities of the THz propagation medium as well as the physical characteristic of the RIS. Building upon this model, we present a comprehensive system model for RIS-assisted THz wireless systems that support broadcasting and we conduct coverage analysis that reveals their limitations. Specifically, the contribution of this paper is as follows:

- We provide a system model for RIS-assisted THz wireless communications and we employ electromagnetic theory tools to derive a general expression for the end-to-end (e2e) channel attenuation. This expression takes into account not only the access point (AP)-RIS and RIS-user equipment (UE) distances, but also the RIS size, the radiation pattern and the reflection coefficient of the RIS unit cell, the AP and UE antenna gain, the transmission frequency, as well as the environmental conditions. Note that they have been two already published contributions that provided the e2e pathloss in RIS-assisted wireless sytsems [55], [56]. However, both [55] and [56] refer to low frequency band communications; thus, they neglect the impact of molecular absorption loss.

- Building upon the channel attenuation expression, we provide a simple closed-form expression that determines the phase shift that each RIS element should impose in order to steer the beam radiated from the RIS towards a desired direction.
- Next, we present a tight channel coefficient approximation that enables the performance analysis of the RIS-assisted THz wireless system.
- Based on the channel coefficient approximation, we present the theoretical framework that returns the cumulative distribution function (CDF) of the e2e channel coefficient of the RIS-assisted THz wireless system. In more detail, we consider a RIS-assisted downlink scenario in which a single AP broadcasts to a number of UEs that are located in random positions within a circular cluster of radius equals to the one of the RIS to center of the cluster footprint, and we obtain closed-form expressions for the e2e channel coefficient CDF.
- Finally, we use the e2e channel statistics to extract an insightful closed-form expression for the coverage probability.

The rest of the paper is structured as follows: Section II focuses on presenting the system and channel model accompanied by the latter's tight approximation, while Section III presents the statistical analysis of the e2e channel coefficient as well as the closed-form expression for the coverage probability. Numerical results verified by respective simulations and accompanied by quantitative assessment are reported in Section IV. Finally, closing remarks and key observations of this work are summarized in Section V.

Notations: The operator $|\cdot|$ respectively denotes the absolute value, whereas $\exp(x)$ stands for the exponential function. Additionally, $\sqrt{x}$ returns the square root of x, while $\sin(\cdot)$, $\cos(\cdot)$, $\sin^{-1}(\cdot)$, $\cos^{-1}(\cdot)$ and $\text{sinc}(\cdot)$ respectively denote the sine, cosine, arc sine, arc cosine, and sinc functions.

II. SYSTEM & CHANNEL MODEL

In this section, we present the system model and we extract general formulas and approximations for the e2e channel coefficient. It is organized as follows: Section II-A presents the system model, while Section II-B reports the channel model.

A. SYSTEM MODEL

As illustrated in Fig. 1, we consider the downlink scenario of a RIS-assisted wireless THz system, in which a single AP serves N_u UE, that form a circular cluster with center $O'(0, 0)$ and radius r_e, through a RIS. Moreover, it is assumed that, due to blockage, no direct link between the AP and UEs can be established. The AP and the n_u-th UE, with $n_u \in \{1, \ldots, N_U\}$ are equipped with high directional antennas of gains G_{AP} and G_{n_u}, respectively, which point at the center of the RIS. The RIS consists of $M \times N$ orthogonal unit cells of dimensions d_x and d_y and it is assumed that it has knowledge concerning the position of the center of the cluster and its radius. Moreover, the AP can use different codebooks in order to adjust its beamwidth and focusing point in the RIS. Based on the the
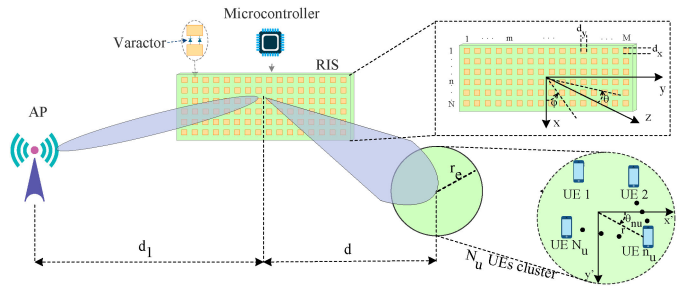

FIGURE 1. System model.

used codebook different size of the RIS, i.e., different number of RUs are employed. This allows the system to adjust the RIS main lobe footprint in order to equal the cluster radius. Notice that this functionality require that the cluster size is known to the AP. A three dimensional (3D) Cartesian system is defined with its center being at the center of the RIS and the RIS to be at its x-y plane. Hence, the position of the RU, $\mathcal{U}_{m,n}$ can be obtained as

$$\mathbf{d}_{m,n} = \left(n - \frac{1}{2}\right) d_x \mathbf{x}_o + \left(m - \frac{1}{2}\right) d_y \mathbf{y}_o + 0\mathbf{z}_o, \quad (1)$$

with $n \in [1 - \frac{N}{2}, \frac{N}{2}]$ and $m \in [1 - \frac{M}{2}, \frac{M}{2}]$. Also, $\mathbf{x}_o$, $\mathbf{y}_o$, and $\mathbf{z}_o$ stand for the unitary vectors at the x, y, and z direction, respectively. Let, $\theta^t_{m,n}$ and θ^r_{m,n,n_u} be the elevation angle from the (m, n) RU, $\mathcal{U}_{m,n}$, to the AP and to the n_u-th UE, respectively, while $\phi^t_{m,n}$ and ϕ^r_{m,n,n_u} stand for the corresponding azimuth angle. Finally, we use $l^t_{m,n}$ and l_{m,n,n_u} to respectively define the distances from AP to the $\mathcal{U}_{m,n}$ RU and the one from the $\mathcal{U}_{m,n}$ RU to the n_u-th UE.

B. CHANNEL MODEL

In this section, we assume that the distance between the center of the RIS and the n_u-th UE is known, and we evaluate the received power at the n_u- th, we identify the optimal phase shift of each $\mathcal{U}_{m,n}$ in order to steer the RIS-generated beam to a desired direction, and we obtain the channel coefficient as a function of the RIS specifications and THz-specific characteristics.

For a given n_u-th UE position, the following theorem returns the received power at the n_u-th UE.

Theorem 1: The received power at the n_u-th UE can be evaluated as

$$P_r = L_{n_u} P_{AP}, \quad (2)$$

where L_{n_u} can be expressed as in (3)

$$L_{n_u} = M^2 N^2 \frac{d_x d_y \lambda^2 |R|^2 U^r (\theta_i, \phi_i) U^t (\theta_r, \phi_r) G_t}{64\pi^3 d_1^2 d_{n_u}^2}$$

$$\times \frac{\text{sinc}^2 \left(\frac{N\pi}{\lambda} \left(\sin (\theta_i) \cos (\theta_i) + \sin (\theta_r) \cos (\phi_r) + \zeta_1\right) d_x\right)}{\text{sinc}^2 \left(\frac{\pi}{\lambda} \left(\sin (\theta_i) \cos (\theta_i) + \sin (\theta_r) \cos (\phi_r) + \zeta_1\right) d_x\right)}$$

$$\times \frac{\text{sinc}^2\left(\frac{M\pi}{\lambda}\left(\sin(\theta_i)\sin(\phi_i)+\sin(\theta_r)\sin(\phi_r)+\zeta_2\right)d_y\right)}{\text{sinc}^2\left(\frac{\pi}{\lambda}\left(\sin(\theta_i)\sin(\phi_i)+\sin(\theta_r)\sin(\phi_r)+\zeta_2\right)d_y\right)}$$

$$\times \exp\left(-\kappa(f)\left(d_1+d_{n_u}\right)\right) \tag{3}$$

In (3),

$$\zeta_1\left(n-\frac{1}{2}\right)d_x + \zeta_2\left(m-\frac{1}{2}\right)d_y = \frac{\lambda\phi_{m,n}}{2\pi}, \tag{4}$$

and

$$G_t = G_{AP}GG_{n_u}. \tag{5}$$

Additionally, $\phi_{m,n}$ and $|R|$ are respectively the controllable phase shift and the absolute value of the reflection coefficient introduced by the (m,n) RU, while $U^r(\theta,\phi)$, $U^t(\theta,\phi)$ and G are the normalized received, the normalized transmitted power ratio patterns and the unit cell gain, respectively. Moreover, d_1 and d_{n_u} represents the AP to the center of the RIS distance and the one from the center of the RIS to the n_u-th UE. Meanwhile, θ_i and ϕ_i are respectively the elevation and the azimuth angles from the center of the RIS to the AP, while θ_r and ϕ_r respectively denotes the elevation and the azimuth angles from the center of the the RIS to the center of the cluster. Finally, in (3), $\kappa(f)$ stands for the molecular absorption coefficient and can be obtained as in (6), [54].[1]

$$\kappa(f) = \frac{A(\mu)}{B(\mu)+\left(\frac{f}{100c}-q_1\right)^2} + \frac{C(\mu)}{E(\mu)+\left(\frac{f}{100c}-q_2\right)^2}$$

$$+ \frac{F(\mu)}{G(\mu)+\left(\frac{f}{100c}-q_3\right)^2} + \frac{I(\mu)}{J(\mu)+\left(\frac{f}{100c}-q_4\right)^2}$$

$$+ \frac{K(\mu)}{L(\mu)+\left(\frac{f}{100c}-q_5\right)^2} + \frac{M(\mu)}{N(\mu)+\left(\frac{f}{100c}-q_6\right)^2}$$

$$+ R(\mu,f) \tag{6}$$

In (6),

$$A(\mu) = a_1\left(1-\mu\right)\left(a_2\left(1-\mu\right)+a_3\right), \tag{7}$$

$$B(\mu) = \left(b_1\left(1-\mu\right)+b_2\right)^2, \tag{8}$$

$$C(\mu) = c_1\mu\left(c_2\mu+c_3\right), \tag{9}$$

$$E(\mu) = \left(e_1\mu+d_2\right)^2, \tag{10}$$

$$F(\mu) = f_1\mu\left(f_2\mu+f_3\right), \tag{11}$$

$$G(\mu) = \left(g_1\mu+g_2\right)^2, \tag{12}$$

$$I(\mu) = i_1\mu\left(i_2\mu+i_3\right), \tag{13}$$

$$J(\mu) = \left(j_1\mu+j_2\right)^2, \tag{14}$$

$$K(\mu) = k_1\mu\left(k_2\mu+k_3\right), \tag{15}$$

$$L(\mu) = \left(l_1\mu+l_2\right)^2, \tag{16}$$

$$M(\mu) = m_1\mu\left(m_2\mu+m_3\right), \tag{17}$$

$$N(\mu) = \left(n_1\mu+n_2\right)^2, \tag{18}$$

$$R(\mu,f) = \frac{\mu}{r_1}\left(r_2+r_3f^{r_4}\right), \tag{19}$$

with $a_1 = 5.159 \times 10^{-5}$, $a_2 = -6.65 \times 10^{-5}$, $a_3 = 0.0159$, $b_1 = -2.09 \times 10^{-4}$, $b_2 = 0.05$, $c_1 = 0.1925$, $c_2 = 0.135$, $c_3 = 0.0318$, $e_1 = 0.4241$, $e_2 = 0.0998$, $f_1 = 0.2251$, $f_2 = 0.1314$, $f_3 = 0.0297$, $g_1 = 0.4127$, $g_2 = 0.0932$, $i_1 = 2.053$, $i_2 = 0.1717$, $i_3 = 0.0306$, $j_1 = 0.5394$, $j_2 = 0.0961$, $k_1 = 0.177$, $k_2 = 0.0832$, $k_3 = 0.0213$, $l_1 = 0.2615$, $l_2 = 0.0668$, $m_1 = 2.146$, $m_2 = 0.1206$, $m_3 = 0.0277$, $n_1 = 0.3789$, $n_2 = 0.0871$, $r_1 = 0.0157$, $r_2 = 2 \times 10^{-4}$, $r_3 = 0.915 \times 10^{-112}$, $r_4 = 9.42$, $q_1 = 3.96$, $q_2 = 6.11$, $q_3 = 10.84$, $q_4 = 12.68$, $q_5 = 14.65$, and $q_6 = 14.94$. Moreover, c is the speed of light, and μ is the volume mixing ratio of the water vapor and can be obtained as

$$\mu = p_1\left(p_2+p_3P\right)\exp\left(\frac{p_4\left(T-p_6\right)}{T+p_5-p_6}\right), \tag{20}$$

where $p_1 = 6.1121$, $p_2 = 1.0007$, $p_3 = 3.46 \times 10^{-8}$, $p_4 = 17.502$, $p_5 = 240.97\,^oK$, and $p_6 = 273.15\,^oK$. Furthermore, T stands for the air temperature, and P is the atmospheric pressure.

Proof: Please refer to Appendix A. ∎

Remark 1: To steer the beam at the desired direction $\theta_r = \theta_o$ and $\phi_r = \phi_o$, the parameters ζ_1 and ζ_2 should be

$$\zeta_1 = -\left(\sin(\theta_i)\cos(\phi_i)+\sin(\theta_o)\cos(\phi_o)\right) \tag{21}$$

and

$$\zeta_2 = -\left(\sin(\theta_i)\sin(\phi_i)+\sin(\theta_o)\sin(\phi_o)\right). \tag{22}$$

In this case, based on (4), the phase shift of the (m,n) element can be obtained as in (23),

$$\phi_{m,n}^o = -\frac{2\pi}{\lambda}\left(n-\frac{1}{2}\right)\left(\sin(\theta_i)\cos(\theta_i)+\sin(\theta_o)\cos(\phi_o)\right)$$

$$d_x - \frac{2\pi}{\lambda}\left(m-\frac{1}{2}\right)\left(\sin(\theta_i)\sin(\theta_i)+\sin(\theta_o)\sin(\phi_o)\right)d_y \tag{23}$$

In this case, according to (3), the maximum path-gain is

$$L_{n_u}^{\max} = M^2N^2\frac{d_xd_y\lambda^2|R|^2U^r(\theta_o,\phi_o)U^t(\theta_o,\phi_o)G_t}{64\pi^3d_1^2d_{n_u}^2}$$

$$\times \exp\left(-\kappa(f)\left(d_1+d_{n_u}\right)\right). \tag{24}$$

---

[1]In order to compute the molecular absorption coefficient, radiative transfer theory [57] and the high resolution transmission molecular absorption (HITRAN) database [58] are widely used. However, since, in practice THz wireless systems are expected to operate in the $100-500$ GHz band, we employ a simplified model for this band, which was introduced in [25] and then extended in [54]. Note that this model, although it is a theoretical one, is heavily based on the HITRAN database, which contains experimental data. In other words, it has been verified by experimental data.

From (24), the channel gain of the received signal at the n_u UE at a specific distance d_{n_u} can be expressed as

$$h_{n_u} = MN \frac{\sqrt{d_x d_y} \lambda |R| \sqrt{U^r(\theta_i, \phi_i) U^t(\theta_r, \phi_r) G_t}}{8\pi^{3/2} d_1 d_{n_u}}$$
$$\times \exp\left(-\frac{1}{2}\kappa(f)(d_1 + d_{n_u})\right). \quad (25)$$

The following Lemma returns a tight approximation of the channel coefficient.

Lemma 1: For realistic scenarios, the channel coefficient can be tightly approximated as

$$h_{n_u} \approx h_{n_u}^l \mathcal{X}, \quad (26)$$

where

$$h_{n_u}^l = MN \frac{\sqrt{d_x d_y} \lambda |R| \sqrt{U^t(\theta_o, \phi_o) U^r(\theta_i, \phi_i) G_t} \kappa(f)}{16\pi^{3/2} d_1}$$
$$\times \exp\left(-\frac{1}{2}\kappa(f)d_1\right). \quad (27)$$

and

$$\mathcal{X} = \frac{2}{\kappa(f)d_{n_u}} - 1. \quad (28)$$

Proof: From (25), the equivalent e2e channel coefficient can be rewritten as

$$h_{n_u} = h_{n_u}^l \mathcal{Y}, \quad (29)$$

where

$$\mathcal{Y} = \frac{\exp\left(-\frac{1}{2}\kappa(f)d_{n_u}\right)}{\frac{1}{2}\kappa(f)d_{n_u}}. \quad (30)$$

Next, by taking into account that, in practice, $\kappa(f) << 0.1$ and by applying the Maclaurin series of the exponential function [59] in (30), $\mathcal{Y}$ can be tightly approximated as

$$\mathcal{Y} \approx \mathcal{X}. \quad (31)$$

Finally, by substituting (31) into (29), we obtain (26). This concludes the proof. ∎

III. PERFORMANCE ANALYSIS
This section is focused on presenting the theoretical framework for the quantification of the coverage performance of the RIS-assisted THz wireless system. In particular, Section III-A present a closed-form expressions for the CDF of the e2e channel coefficient, whereas, Section III-B, builds upon this expression and extract a novel closed-form formula for the coverage probability.

A. STATISTICAL ANALYSIS OF THE CHANNEL COEFFICIENT
We assume that the RIS is placed at height L_R from the n_u−th UE and that it targets at (ϕ_o, θ_o). In the far-field, the euclidean distance between the center of the RIS and the n_u UE can be

approximated as

$$d_{n_u} \approx d - r_{n_u} \cos\left(\theta_{n_u}\right), \quad (32)$$

where d is the euclidean distance between the center of the RIS and the center of the cluster, r_{n_u} is the distance of the n_u UE from the center of the cluster and θ_{n_u} is the physical direction of the n_u UE with respect to the coordination system defined by the center of the cluster. Note that the UE location is uniformly distribution in a disc of radius r_e; hence, the probability density function of r_{n_u} can be obtained as

$$f_{r_{n_u}}(r) = \frac{2r}{r_e^2}, \text{ with } r \in [0, r_e]. \quad (33)$$

Moreover, θ_{n_u} can be modeled as a uniform distribution with probability density function (PDF) that can be expressed as

$$f_{\theta_{n_u}}(x) = \frac{1}{2\pi}, \text{ with } x \in [0, 2\pi]. \quad (34)$$

Finally, note that r_{n_u} and θ_{n_u} are independent.

The following theorem returns the PDF and the CDF of the random variable

$$\mathcal{Z} = r_{n_u} \cos\left(\theta_{n_u}\right). \quad (35)$$

Theorem 2: The PDF and CDF of $\mathcal{X}$ can be respectively obtained as

$$f_{\mathcal{Z}}(x) = \frac{2\sqrt{r_e^2 - x^2}}{\pi r_e^2}, \text{ with } x \in [-r_e, r_e] \quad (36)$$

and

$$F_{\mathcal{Z}}(x) = \begin{cases} 0, & x \leq -r_e \\ \frac{1}{2} + \frac{1}{\pi}\left[\frac{x\sqrt{r_e^2 - x^2}}{r_e^2} + 2\sin^{-1}\left(\frac{x}{r_e}\right)\right], & -r_e < x < r_e \\ 1, & x \geq r_e \end{cases} \quad (37)$$

Proof: Please refer to Appendix B. ∎

The following theorem returns the CDF of d_{n_u}.

Theorem 3: The CDF of d_{n_u} can be expressed as in (38), given at the top of the next page.

$$F_{d_{n_u}}(x) = \begin{cases} 0, & x < d - r_e \\ \frac{1}{2} - \frac{1}{\pi}\left[\frac{(d-x)\sqrt{r_e^2 - (d-x)^2}}{r_e^2}\right. & d - r_e \leq x \leq r_e + d \\ \left. -2\sin^{-1}\left(\frac{d-x}{r_e}\right)\right], & \\ 1, & x \geq d + r_e \end{cases} \quad (38)$$

Proof: Please refer to Appendix C. ∎

The following theorem returns the CDF of the e2e channel coefficient, assuming that the UE is located within the maximum path-gain region.[2]

---

[2] As maximum path-gain region, we define the area in which the following condition holds: $|L_{n_u}/L_{n_u}^{\max}| < \epsilon$, where ϵ stands for the maximum acceptable path-gain reduction in comparison with $L_{n_u}^{\max}$.

Theorem 4: Assuming that the UE is located within the maximum path-gain region, the CDF of the e2e channel coefficient can be obtained as in (39),

$$F_{h_{n_u}}(x) = \begin{cases} 0, & x < h_{n_u}^l \left(\frac{2}{\kappa(f)(d+r_e)} - 1 \right) \\[2ex] \frac{1}{2} + \frac{1}{\pi} \frac{\left(d - \frac{2h_{n_u}^l}{\kappa(f)\left(x+h_{n_u}^l\right)} \right) \sqrt{r_e^2 - \left(d - \frac{2h_{n_u}^l}{\kappa(f)\left(x+h_{n_u}^l\right)}\right)^2}}{r_e^2} \\[2ex] + 2\sin^{-1}\left(\frac{d - \frac{2h_{n_u}^l}{\kappa(f)\left(x+h_{n_u}^l\right)}}{r_e} \right), \\[2ex] \qquad h_{n_u}^l \left(\frac{2}{\kappa(f)(d+r_e)} - 1 \right) \leq x \leq h_{n_u}^l \left(\frac{2}{\kappa(f)(d-r_e)} - 1 \right) \\[2ex] 1, & x \geq h_{n_u}^l \left(\frac{2}{\kappa(f)(d-r_e)} - 1 \right) \end{cases} \tag{39}$$

Proof: Please refer to Appendix D. ∎

B. COVERAGE PROBABILITY

As coverage probability, we define the probability that the received power at the n_u-th UE that is within the maximum path-gain region, to be above a predetermined threshold P_{th}, i.e.,

$$P_c = \Pr\left(P_r \geq P_{th} \,|\, r_e = r_{th}\right), \tag{40}$$

where r_{th} denotes the radius of the maximum path-gain region. Note that different applications require different levels of minimum achievable spectral efficiency, which can be defined as

$$C = \log_2\left(1 + \frac{P_r}{N_o}\right), \tag{41}$$

where N_o stands for the noise power. Thus, for a spectral efficiency requirement, C_{th}, the received power should be at least equal to P_{th}. Hence, (41) can be rewritten as

$$C_{th} = \log_2\left(1 + \frac{P_{th}}{N_o}\right), \tag{42}$$

or equivalently

$$P_{th} = \left(2^{C_{th}} - 1\right) N_o. \tag{43}$$

The following theorem returns a closed-form expression for the coverage probability.

Theorem 5: The coverage probability can be obtained as in (44),

$$P_c = \begin{cases} 1, & P_{th} < \left(h_{n_u}^l\right)^2 \left(\frac{2}{\kappa(f)(d+r_{th})} - 1 \right)^2 P_{AP} \\[2ex] \frac{1}{2} - \frac{1}{\pi} \frac{\left(d - \frac{2h_{n_u}^l}{\kappa(f)\left(\sqrt{\frac{P_{th}}{P_{AP}}}+h_{n_u}^l\right)}\right) \sqrt{r_{th}^2 - \left(d - \frac{2h_{n_u}^l}{\kappa(f)\left(\sqrt{\frac{P_{th}}{P_{AP}}}+h_{n_u}^l\right)}\right)^2}}{r_{th}^2} \\[2ex] \quad - 2\sin^{-1}\left(\frac{d - \frac{2h_{n_u}^l}{\kappa(f)\left(\sqrt{\frac{P_{th}}{P_{AP}}}+h_{n_u}^l\right)}}{r_{th}} \right), \\[2ex] \qquad \left(h_{n_u}^l\right)^2 \left(\frac{2}{\kappa(f)(d+r_{th})} - 1 \right)^2 P_{AP} \leq P_{th} \leq \left(h_{n_u}^l\right)^2 \\[2ex] \qquad \left(\frac{2}{\kappa(f)(d-r_{th})} - 1 \right)^2 P_{AP} \\[2ex] 0, & P_{th} \geq \left(h_{n_u}^l\right)^2 \left(\frac{2}{\kappa(f)(d-r_{th})} - 1 \right)^2 P_{AP} \end{cases} \tag{44}$$

In (44),

$$r_{th} < \frac{2}{\kappa(f)} - d, \tag{45}$$

otherwise, $P_c = 0$.

Proof: Please refer to Appendix E. ∎

Remark 2: From Theorem 5, it becomes evident that in order to achieve a coverage probability that equals 1, a minimum transmission power, which can be evaluated as

$$P_{AP}^{\min} = P_{th} \left(h_{n_u}^l\right)^{-2} \left(\frac{2}{\kappa(f)(d+r_{th})} - 1 \right)^{-2}, \tag{46}$$

should be used.

IV. NUMERICAL RESULTS & DISCUSSION

In this section, we report numerical results, accompanied by related discussions, which highlight the effectiveness of RIS-assisted THz wireless systems, reveals their limitations as well as the relationship with the system parameters and performance. In this direction, unless otherwise stated, we investigate the following insightful scenario. We consider standard environmental conditions, i.e., relative humidity 50%, atmospheric pressure 101325 Pa, and temperature 296°K. The AP transmission antenna gain is 50 dBi, which according to [30], [60], [61] is a realistic value for THz wireless systems, while the UE received antenna gains are 20 dBi. The antenna pattern of the RUs is described by [62], [63]

$$U(\theta, \phi) = \begin{cases} \cos(\theta), & \theta \in [0, \frac{\pi}{2}] \text{ and } \phi \in [0, 2\pi] \\ 0, & \text{otherwise.} \end{cases} \tag{47}$$

Thus, G can be obtained as

$$G = \int_0^{2\pi} \int_0^{\frac{\pi}{2}} U(\theta, \phi) \sin(\theta) \, d\theta d\phi, \tag{48}$$

which by substituting (47) and performing the integration returns $G = 4$. Moreover, $|R|$ is set to 0.9, which is in-line
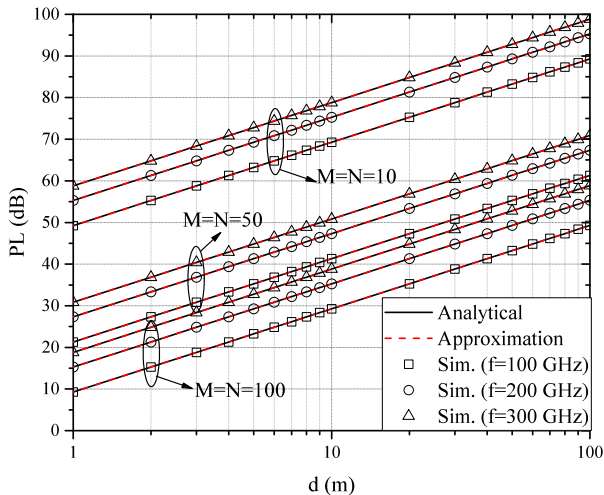
FIGURE 2. PL vs *d* for different values of $M = N$ and *f*.

with [64]. The cluster radius can be obtained as

$$r_e = d \sin\left(\frac{1}{2}\theta_{\mathrm{HP}}\right), \tag{49}$$

where θ_{HP} stands for the azimuth half-power beamwidth (AHPB) of the RIS. Finally, without loss of generality, we assume that $N_u = 1$. Of note, in what follows, we use continuous lines and markers to respectively denote theoretical and simulation results. Additionally, we employ the finite element method (FEM) in order to verify the channel model. Notice that this approach has been previously used in several published contributions (see e.g., [65], [66] and reference therein), due to its capability to accurate model electromagnetic propagation mechanisms. Finally, respective Monte Carlo simulations are employed to verify the coverage probability theoretical framework.

In Fig. 2, the PL is demonstrated as a function of the RU to the center of cluster distance for different values of transmission frequency and $M = N$, assuming that $d_1 = 1$ m and that the optimal phase shifts are performed by each RU of the RIS. In this figure, continuous lines are used to represent the PL derived by (24), while dashed lines are employed to denote the PL approximation, which is evaluated according to (26). Finally, markers denotes FEM-based simulations. We observe that the PL approximation perfectly match the analytical frameworks; thus, the approximation framework is verified. Moreover, both the analytical and approximated results concise with the simulations, which verifies the PL evaluation framework. As expected, for fixed f and $M = N$, as d increases, the PL also increases. For instance, for $f = 300$ GHz and $M = N = 100$, the PL increases by about 20 dB, as d changes from 1 to 10 m. Moreover, for given d and $M = N$, as f increases, the PL also increases. For example, for $M = N = 10$ and $d = 10$ m, the PL increased by approximately 10 dB, as f increases from 100 to 300 GHz. Finally, we observe that, for fixed f and d, the PL decreases

as the number of RUs increases. For instance, for $d = 10$ m, and $f = 100$ GHz, the PL decreases by approximately 40 dB, as the $M = N$ increases from 10 to 100.

Figure 3 demonstrates the e2e PL as a function of the $n_u - th$ UE direction, for different size of RIS, assuming that $d_1 = d_{nu} = 1$ m, the transmission frequency, $f = 100$ GHz, $d_x = d_y = 0.3$ mm, $|R| = 0.9$, $G_{AP} = 50$ dBi, $G_{nu} = 20$ dBi, $\theta_i = \frac{\pi}{4}$, $\phi_i = \pi$, and no phase shifting is introduced by any RU. Of note the results presented in this figure has been verified by FEM-based simulations. However, for the sake of readability no markers have been placed. Notice that this special case can be considered as RIS performance benchmark and it represents scenarios in which the direction of the $n_u - th$ UE is unknown to the RIS. Figure 3.a illustrates the e2e PL as a function of ϕ_r, for different number of $M = N$, and $\theta_r = \frac{\pi}{4}$. From this figure, we observe that, for given $M = N$, the PL is minimized for $\phi_r = 0^o$. This is in-line with (3) and (4), where, for the special case in which $\phi_{m,n} = 0$, it can be extracted that $\zeta_1 = \zeta_2 = 0$ and that, for $\theta_i \neq 2k\pi$, $\phi_i \neq 2k\pi$, and $\theta_r \neq 2k\pi$, with k integer, the path-gain is maximized for $\phi_r = 2k\pi$. Moreover, it becomes apparent that as $M = N$ increases, the minimum PL decreases. For example, for $M = N = 10$, the minimum e2e PL equals 42.83 dB, while, for $M = N = 10$, it is 2.83 dB. However, as the RIS size increases, the azimuth AHPB decreases. For instance, for $M = N = 10$, the AHPB is approximately equal to 74°, which results to a cluster with radius that is equal to 0.6 m whereas, for $M = N = 100$, it is about 8°, which result to a cluster radius of 7 cm. This indicates that as the RIS size increases, or equivalently as the number of the used RUs increases, the size of the cluster that can be served, decreases. Of note, from (49), it becomes evident that as d increases, r_e also increases. For example, for $d = 10$ m, in the case in which $M = N = 100$, the cluster radius becomes equal to 0.7 m, while, in the case in which $M = N = 10$, it is equal to 6 m. Similarly, Fig. 3.b depicts the e2e PL as a function of θ_r, for different number of $M = N$, and $\phi_r = \frac{\pi}{4}$. Again, as the RIS size increases, the minimum PL and the elevation half-power beamwidth (EHPB) decrease. Meanwhile, Fig. 3.c presents the PL as a function of ϕ_r for $\theta_r = \frac{\pi}{4}$, assuming that $\theta_o = \pi/6$, $\phi_o = \pi/3$ and that the phase shifting of each element is provided according to (23), whereas, in Fig. 3.d, the corresponding PL against θ_r, for $\phi_r = \frac{\pi}{4}$ is depicted. By comparing Fig. 3.a with Fig. 3.c and Fig. 3.b with Fig. 3.d, we observe that by imposing appropriate phase shifting to each RIS RU, the PL pattern is rotated in order to achieve the minimum PL at the desired direction.

In Fig. 4, the PL is presented as a function of the $n_u - th$ UE direction, for different transmission frequencies, assuming that $d_1 = d_{nu} = 1$ m, $d_x = d_y = 0.3$ mm, $|R| = 0.9$, $G_{AP} = 50$ dBi, $G_{nu} = 20$ dBi, $\theta_i = \frac{\pi}{4}$, $\phi_i = \pi$, $\theta_o = \pi/6$, and $\phi_o = \pi/3$. As expected the minimum PL is observed for $\phi_r = \pi/3$. Moreover, it is apparent that for a fixed ϕ_r, as the transmission frequency increases, the PL also increases. Finally, we observe that as the transmission frequency increases, the AHPB decreases.
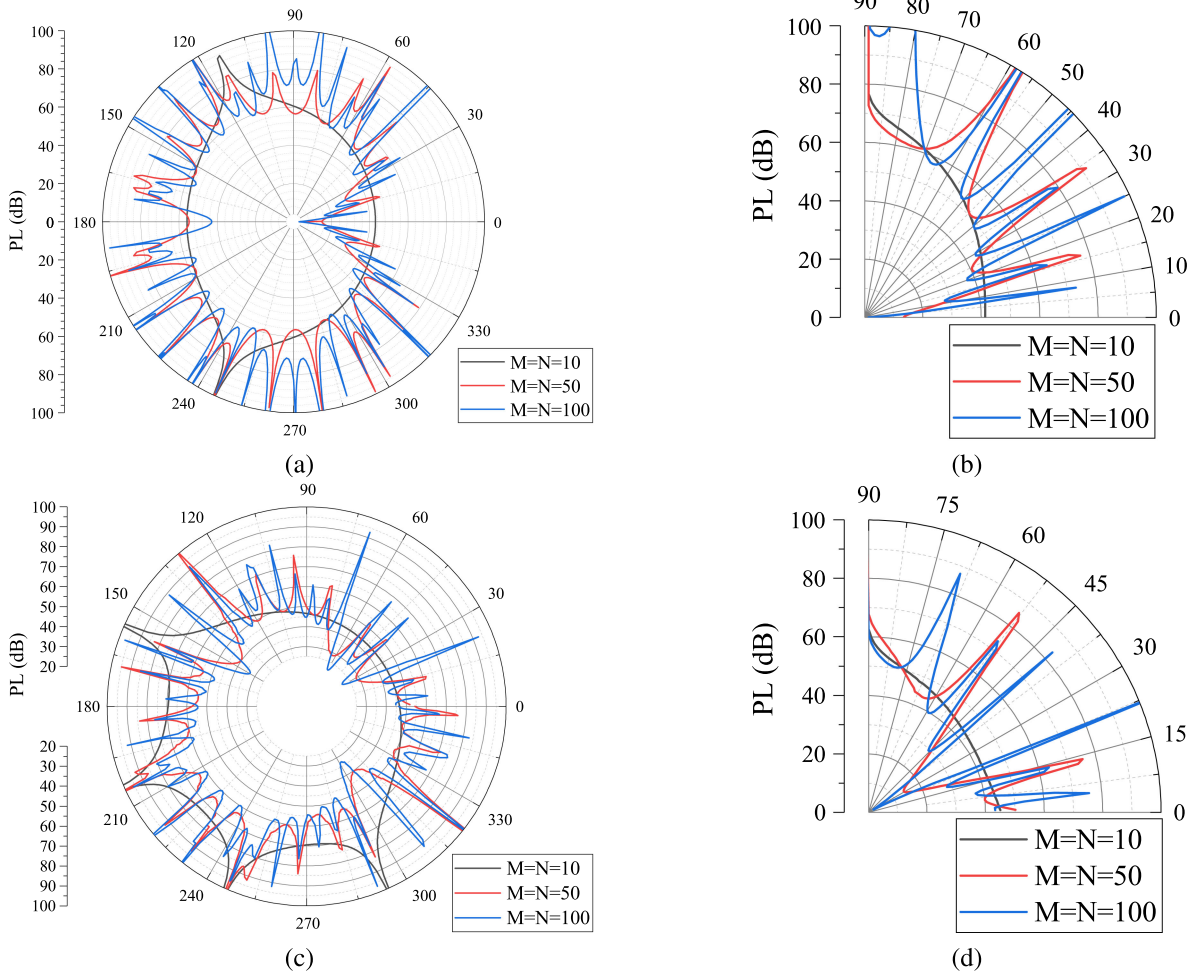
FIGURE 3. a) PL vs ϕ_r, for $\theta_r = \frac{\pi}{4}$ and $\phi_{m,n} = 0^o$, for all m and n, b) PL vs θ_r, for different $\phi_r = \frac{\pi}{4}$ and $\phi_{m,n} = 0^o$, for all m and n. c) PL vs ϕ_r, for $\theta_r = \frac{\pi}{4}$, $\theta_o = \pi/6$, and $\phi_o = \pi/3$. d) PL vs θ_r, for $\phi_r = \frac{\pi}{4}$, $\theta_o = \pi/6$, and $\phi_o = \pi/3$.
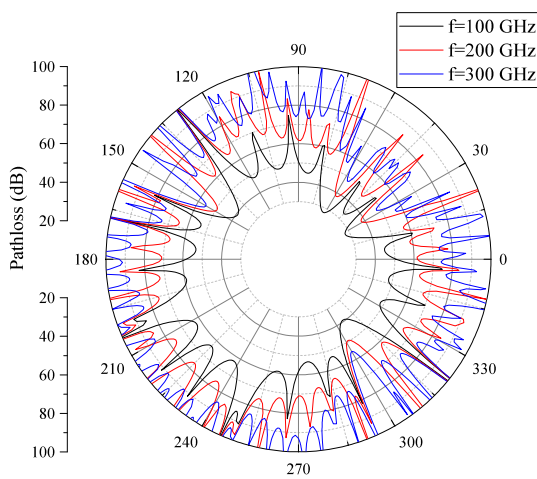

FIGURE 4. PL vs ϕ_r, for $\theta_r = \frac{\pi}{4}$, $\theta_o = \pi/6$, $\phi_o = \pi/3$, and different values of f.
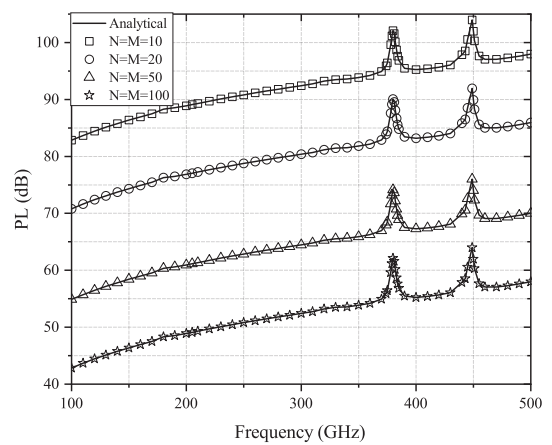

FIGURE 5. PL vs f for different RIS sizes.

Figure 5 depicts the PL as a function of f for different values of $M = N$, assuming that $\theta_i = \theta_r = \theta_o = \phi_r = \phi_o = \frac{\pi}{4}$,

$\phi_i = \frac{3\pi}{4}$, $d_1 = d_{n_u} = 10$ m, and $d_x = d_y = 0.3$ mm. The theoretical results perfectly match the simulations, verifying the proposed channel model. From this figure, it is revealed that
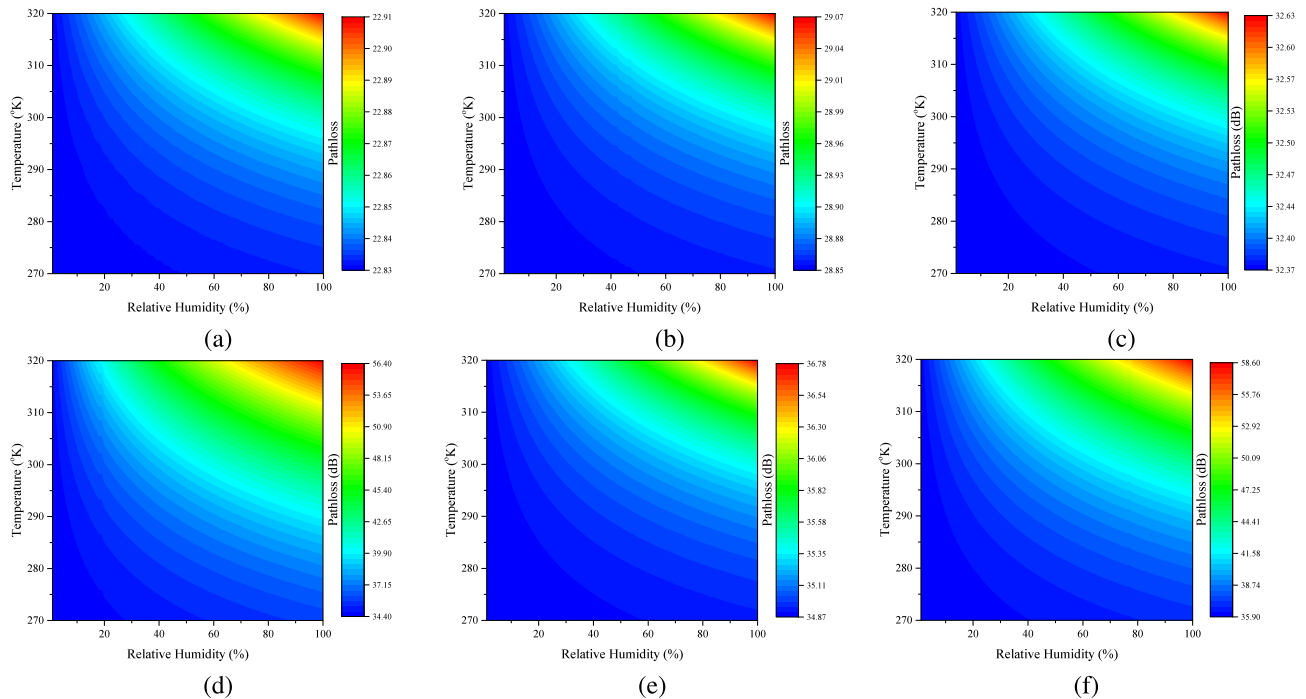
FIGURE 6. PL vs temperature and relative humidity, for (a) $f = 100$ GHz, (b) $f = 200$ GHz, (c) $f = 300$ GHz, (d) $f = 380$ GHz, (e) $f = 400$ GHz, and (f) $f = 450$ GHz.

there exists two frequency regions, the first one from 370 to 390 GHz and the second one from 430 to 455 GHz, in which the PL is maximized. This is due to water molecules resonance. In other words, from 100 to 500 GHz, there exists three transmission windows; the first one from 100 to 365 GHz, the second one from 375 to approximately 430 GHz, and the third one from 460 to 500 GHz. Outside these regions, for fixed M and N, as the transmission frequency increases, the PL also increases. For example, for $M = N = 20$, as f increases from 100 to 300 GHz, the PL increases for about 10 dB. Finally, it is observed that, for a given transmission frequency, as the RIS size increases, the PL decreases. For example, as $M = N$ increases from 10 to 100, the PL decreases for about 40 dB.

In Fig. 6, the PL is plotted as a function of the atmospheric temperature and relative humidity, for different values of f, assuming $M = N = 100$, $d_1 = 1$ m, $d_{n_u} = 10$ m, $d_x = d_y \approx 0.3$ mm, $\theta_i = 45^o$, $\phi_i = 180^o$, and $\theta_r = \theta_o = \phi_r = \phi_o = 45^o$. In more detail, in Fig. 6.a, f is set to 100 GHz, while, in Fig. 6.b, it equals 200 GHz. Likewise, in Fig. 6.c, f is 300 GHz, whereas, in Fig. 6.d, the transmission frequency is set to 380 GHz, which is one of the worst scenarios, since it is one of the resonant frequencies of water molecules. Furthermore, in Fig. 6.e, the transmission frequency is equal to 400 GHz, while, in Fig. 6.f, it is set to 450 GHz that is one of the worst scenarios, due to the fact that in this frequency the molecular absorption in maximized. Notice that, according to [67]–[69], the frequencies 100, 200, 300 and 400 GHz are within the THz transmission windows. As expected, for
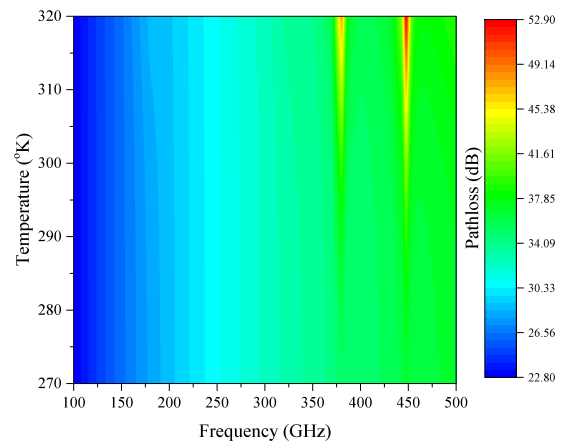

FIGURE 7. PL vs temperature and frequency.

a fixed atmospheric temperature, as the humidity increases, the water molecules increases; thus, the molecular absorption and the PL increase. For instance, in the worst case scenario in which $f = 380$ GHz, for an atmospheric temperature of 273^oK, the PL increases by approximately 2 dB as relative humidity increases from 10% to 90%. On the other hand, for $f = 100$ GHz, for the same atmospheric temperature, the PL increase does not surpass 0.25 dB as the relative humidity changes from 10% to 90%. The aforementioned examples reveals the importance of taking into account both the transmission frequency and the atmospheric conditions, when
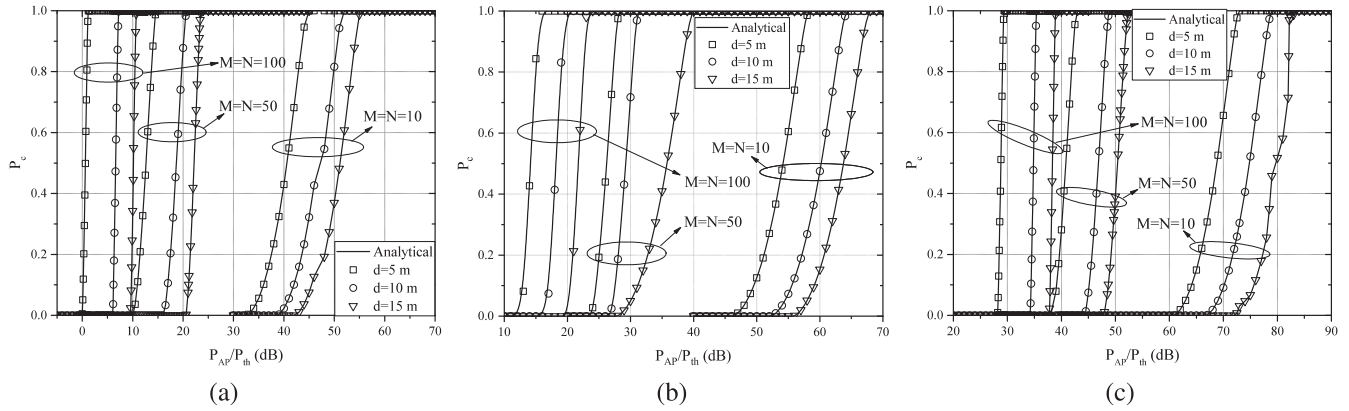
FIGURE 8. P_c vs P_{AP}/P_{th} for different RIS sizes and d, assuming a) $f = 100$ GHz, b) $f = 200$ GHz, and c) $f = 300$ GHz.
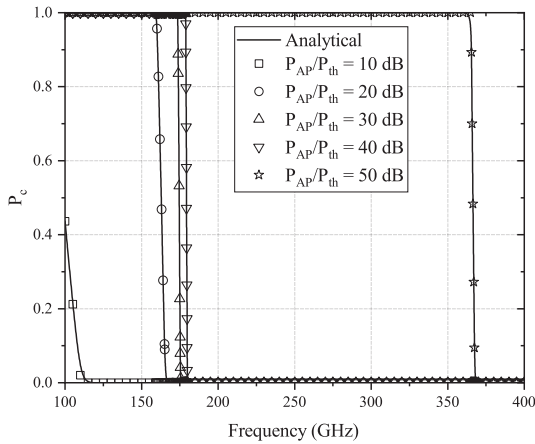

FIGURE 9. P_c vs frequency for different P_{AP}/P_{th}.

evaluating the link budget of of RIS-assisted THz systems. Similarly, for a given relative humidity, as the atmospheric temperature increases, the PL also increases. For example, for $f = 380$ GHz and a relative humidity equals 50%, the PL increases by 2 dB as the atmospheric temperature increase from $270^o K$ to $290^o K$. On the contrary, for $f = 100$ GHz, the same relative humidity, the PL increases by approximately 0.01 dB as the atmospheric temperature increase from $270^o K$ to $290^o K$. Moreover, for $f = 200$ GHz, the same temperature variation causes a PL increase in the range of 0.05 dB, while, for $f = 400$ GHz, it results to 0.5 dB. This indicates that as the frequency increases the impact of environmental conditions to the PL become more severe. Finally, from this figure, it becomes evident that neglecting the absorption loss would lead to a frequency-dependent PL error in the range of [0.1, 22.7 dB]. This highlights the importance of taking into account the molecular absorption loss when evaluating the PL and the performance of RIS-assisted THz systems.

Figure 7 illustrates the PL as a function of the air temperature and the transmission frequency, assuming $M = N = 100$, $d_1 = 1$ m, $d_{n_u} = 10$ m, $d_x = d_y \approx 0.3$ mm, $\theta_i = 45^o$, $\phi_i =$

180°, and $\theta_r = \theta_o = \phi_r = \phi_o = 45^o$. As expected, for a given transmission frequency, as the air temperature increases, the PL also increases. For example, for $f = 250$ GHz, the PL increases by about 0.1 dB, as the air temperature increases from 270 to $320^o K$. Moreover, from this figure, it is verified that there exist two frequency regions in which the PL is maximized. In these regions, temperature variations cause a more severe impact on PL. For instance, increasing the air temperature from 270 to $280^o K$ results in 0.02 dB PL increase, if the transmission frequency is equal to 280 GHz, while, the same temperature increase cause a 0.5 dB PL increase, when the transmission frequency is set to 383 GHz. This indicates the importance of taking into account the air temperature and its variations, when selecting the transmission frequency.

Figure 8 presents the coverage probability as a function of P_{AP}/P_{th}, for different values of f, $M = N$ and d, assuming that $\phi_i = \pi$, $\phi_r = 0$, and $\theta_i = \theta_r = \frac{\pi}{4}$. From this figure, we observe that the analytical results coincide with the simulations, verifying the derived expressions. Moreover, for given f, $M = N$ and d, as $\frac{P_{AP}}{P_{th}}$ increases, the coverage probability also increases. For example, for $f = 200$ GHz, $M = N = 10$ and $d = 5$ m, P_c increases from 12.6% to 60.5%, as P_{AP}/P_{th} increases from 50 to 55 dB. Meanwhile, for fixed d and $\frac{P_{AP}}{P_{th}}$, although, as the RIS size increase, r_{th} decreases, the path-gain increases; hence, the P_c also increases. For instance, for $f = 200$ GHz, $d = 5$ m and $\frac{P_{AP}}{P_{th}} = 40$ dB, as $M = N$ increases from 10 to 50, r_{th} decreases from approximately 6.02 to 2.59 m; however, P_c increases from 0 to 1. Additionally, we observe that for given RIS size and $\frac{P_{AP}}{P_{th}}$, as d increases, P_c decreases. Finally, by comparing Figs. 8 a-c, it becomes apparent that for given $\frac{P_{AP}}{P_{th}}$, $M = N$ and d, as f increases, the P_c decreases. For example, for $M = N = 50$, $d = 15$ m, and $\frac{P_{AP}}{P_{th}} = 25$ dB, P_c reduces from 1 to 0 as the transmission frequency changes from 100 to 300 GHz.

Figure 9 depicts the coverage probability as a function of the transmission frequency, for different values of $\frac{P_{AP}}{P_{th}}$, assuming $M = N = 100$, $\phi_i = \pi$, $\phi_r = 0$, $\theta_i = \theta_r = \frac{\pi}{4}$ and $d = 15$ m. As expected, for a given $\frac{P_{AP}}{P_{th}}$, as the transmission frequency increases, the PL increases; thus, the coverage
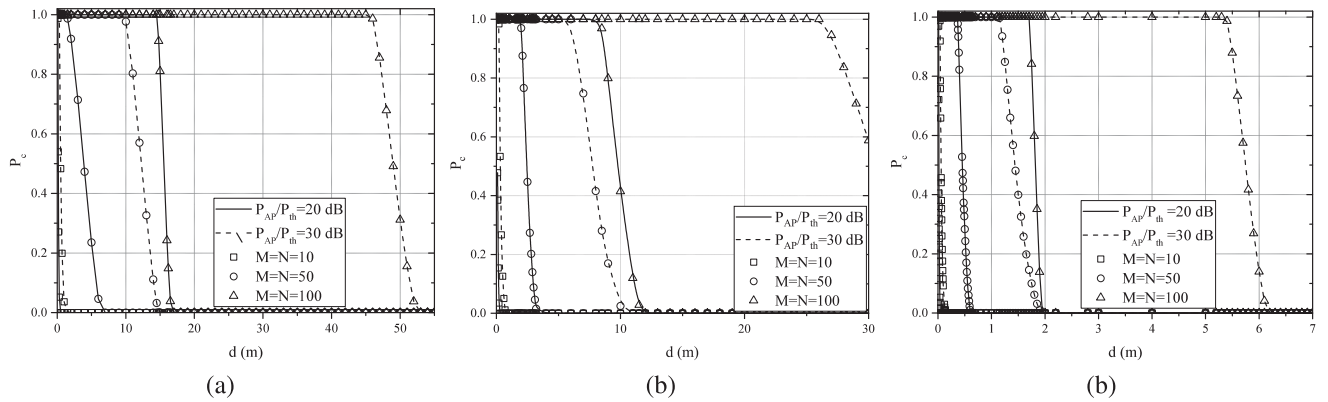
FIGURE 10. P_c vs d for different values of P_{AP}/P_{th} and RIS size, assuming a) $f = 100$ GHz, b) $f = 200$ GHz, and c) $f = 300$ GHz.
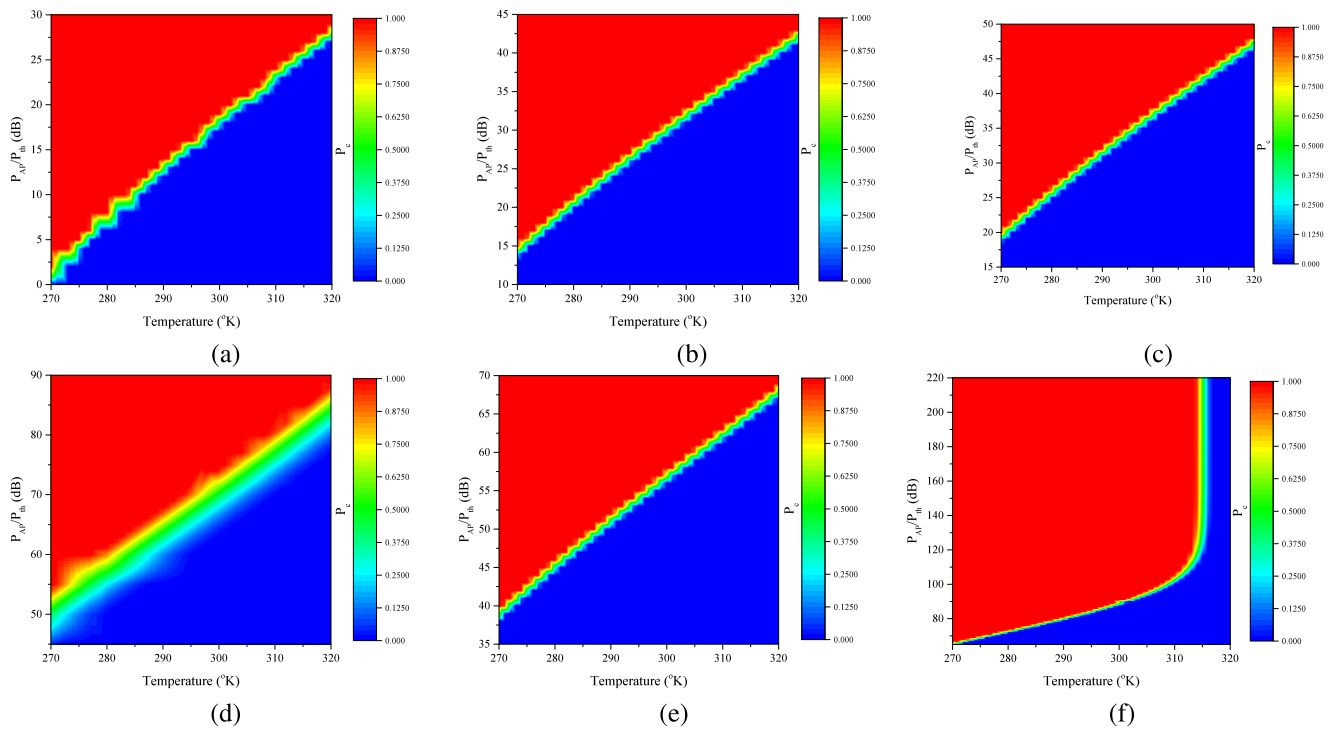

FIGURE 11. P_c vs T and P_{AP}/P_{th}, assuming a) $f = 100$ GHz, b) $f = 200$ GHz, c) $f = 300$ GHz, d) $f = 380$ GHz, e) $f = 400$ GHz and f) $f = 450$ GHz.

probability decreases. Likewise, for a fixed transmission frequency, as $\frac{P_{AP}}{P_{th}}$ increases, the received power increases; as a result, the coverage probability also increases. For example, for a transmission frequency that is equal to 250 GHz, as $\frac{P_{AP}}{P_{th}}$ increases from 40 to 50 dB, the coverage probability increases from 0 to 1. Finally, from this figure, it becomes evident that as $\frac{P_{AP}}{P_{th}}$ increases, the range of frequencies for which the coverage probability equals 1 increases.

Figure 10 presents the coverage probability as a function of d, for different values of P_{AP}/P_{th}, RIS size, and a) $f = 100$ GHz, b) $f = 200$ GHz, and c) $f = 300$ GHz, assuming $\phi_i = \pi$, $\phi_r = 0$, and $\theta_i = \theta_r = \frac{\pi}{4}$. As expected, for given transmission frequency, RIS size and $\frac{P_{AP}}{P_{th}}$, as d increases,

the average PL increases; thus, the coverage probability decreases. For example, for $f = 200$ GHz, $M = N = 50$ and $\frac{P_{AP}}{P_{th}} = 30$ dB, the coverage probability reduces from 1 to 0, as d increases from 5 to 10 m. Similarly, for $f = 100$ GHz, $M = N = 50$ and $\frac{P_{AP}}{P_{th}} = 30$ dB, P_c changes from 1 to 0, as d increases from 10 to 15 m. Moreover, we observe that by increasing the RIS size, we can counterbalance the transmission distance restriction. For instance, for $f = 200$ GHz, $\frac{P_{AP}}{P_{th}} = 30$ dB, and $d = 20$ m, P_c increases from 0 to 1 as $M = N$ changes from 50 to 100. Likewise, it is observed that for fixed transmission frequency, RIS size and d, as P_{AP}/P_{th} increases, the coverage probability also increases. For example, for $f = 200$ GHz, $d = 10$ m and $M = N = 100$, as

P_{AP}/P_{th} increases from 20 to 30 dB, the coverage probability changes from approximately 40% to 100%. This indicates that another approach to countermeasure the transmission distance restriction is to increase the AP transmission power. Finally, within the same transmission window, for fixed $\frac{P_{AP}}{P_{th}}$, $M = N$, and d, P_c increases as the transmission frequency decreases. For example, for $\frac{P_{AP}}{P_{th}} = 30$ dB, $M = N = 100$, and $d = 40$ m, P_c changes from 0 to 1, as f decreases from 200 to 100 GHz. This reveals that another approach to increase the transmission distance is to decrease the transmission frequency.

Figure 11 depicts the coverage probability as a function of P_{AP}/P_{th} and air temperature for different values of f, assuming $M = N = 100$, $\phi_i = \pi$, $\phi_r = 0$, and $\theta_i = \theta_r = \frac{\pi}{4}$. As expected, for a given temperature as P_{AP}/P_{th} increases, the coverage probability increases. Moreover, for a fixed P_{AP}/P_{th}, as the air temperature increases, the PL increases; hence, the coverage probability decreases. For example, for $f = 380$ GHz and $P_{AP}/P_{th} = 60$ dB, the coverage probability decreases from 1 to 0, as the air temperature increases from 270 to $300^o K$. Similarly, for $f = 100$ GHz and $P_{AP}/P_{th} = 5$ dB, as the temperature changes from 270 to 280 ^{o}K, P_c decreases from 1 to 0. Finally, from this figure it becomes evident that the minimum transmission power that is required to achieve a coverage probability that is equal to 1, increases as the air temperature increases.

V. CONCLUSION

This contribution presented a theoretical framework for RIS-assisted THz wireless system coverage performance evaluation. In more detail, we described the system model and we employed electromagnetic theory tools in order to extract a generalized formula for the e2e path-gain. This formula revealed the relationships between the RIS specifications, namely size, number of RIS RUs, RU size and reflection coefficient, RU's radiation patterns, as well as phase shift of each RU, the transmission parameters, such as transmission frequency AP to center of RIS and center of RIS to UE distance, AP transmission and UE reception antenna gains, azimuth and elevation angles from the AP to the center of the RIS as well as from the center of the RIS to the UE, and THz-specific parameters, like the environmental conditions that affect the molecular absorption. Building upon this expression, we determined the optimal phase shift of each RU in order to steer the RIS-generated beam to a desired direction. Next, we obtained an exact expression for the e2e channel coefficient as well as a tight approximation that allows us to quantify the system performance. Based on this expression, we first obtained the statistics of the e2e channel, we defined the coverage probability of the RIS-assisted THz wireless system and derived a novel closed-form and insightful expression for its quantification. This expression revealed that there exists a minimum AP transmission power that can guarantee a coverage probability of 100%. This minimum AP transmission power depends not only on the system's characteristics, but also on the environmental conditions. Finally, we verified the accuracy of the theoretical framework through respective simulations, which highlighted the dependency between the transmission power and maximum bandwidth that can be used in RIS-assisted THz systems. The results highlight the importance of taking into account the molecular absorption loss when evaluating the PL and the performance of RIS-assisted THz wireless systems. Therefore, this work is expected to contribute on analyzing, simulating, and designing RIS-assisted THz systems. Moreover, it is expected to play a key role on devising physical layer and medium access control algorithms in RIS-assisted THz systems.

The performance analysis of RIS-assisted THz wireless systems were conducted under the assumptions that (i) the center of the cluster is perfectly known to the RIS controller, and (ii) the cluster radius is perfectly known to the AP. It would be interesting to relax the aforementioned assumptions and present new evaluation investigation assuming partial knowledge of the cluster center and radius. Moreover, the fading characteristics should be taken into account. Motivated by this, our future effort will focus on the study of RIS-assisted THz system performance in fading environments under partial cluster position and radius knowledge. Finally, inspired by the fact that in several realistic scenarios the users are mobile and since the proposed path-loss model can be also applied in this scenario, we intend to provide the theoretical framework for quantifying the performance of RIS-assisted THz systems that operate in dynamic environments in which the UEs are mobile.

APPENDICES
A. PROOF OF THEOREM 1

Since $l_{m,n}^t >> \lambda$, where λ is the wavelength of the transmission signal, the power of the incident signal into the $\mathcal{U}_{m,n}$ can be obtained as

$$P_{m,n}^i = \exp\left(-\kappa(f)l_{m,n}^t\right) \frac{G_{AP}P_{AP}}{4\pi\left(l_{m,n}^t\right)^2} U^r\left(\theta_{m,n}^t, \phi_{m,n}^t\right) S_{\mathcal{U}},$$

(50)

where $S_{\mathcal{U}}$ stand for the aperture of the RIS unit cell and can be expressed as

$$S_{\mathcal{U}} = d_x d_y.$$

(51)

By substituting (51) into (50), we can express the power of the incident signal as

$$P_{m,n}^i = \exp\left(-\kappa(f)l_{m,n}^t\right) U^r\left(\theta_{m,n}^t, \phi_{m,n}^t\right) \frac{G_{AP}P_{AP}}{4\pi\left(l_{m,n}^t\right)^2} d_x d_y.$$

(52)

Hence, the electric field of the incident signal into $\mathcal{U}_{m,n}$ can be written as

$$E_{n,m}^i = \sqrt{\frac{2Z_o P_{m,n}^i}{d_x d_y}} \exp\left(-j\frac{2\pi l_{m,n}^t}{\lambda}\right),$$

(53)

where Z_o is the air characteristic impedance.

Based on the energy conversation law, the total reflected signal power by the $\mathcal{U}_{mn}$ unit cell can be obtained as

$$P_{m,n}^r = R_{m,n}^2 P_{m,n}^i. \tag{54}$$

or equivalently

$$P_{m,n}^r = \exp\left(-\kappa(f)l_{m,n}^t\right) \frac{d_x d_y}{4\pi \left(l_{m,n}^t\right)^2} |R_{m,n}|^2$$
$$\times U^r\left(\theta_{m,n}^t, \phi_{m,n}^t\right) G_{AP} P_{AP}. \tag{55}$$

By assuming that $l_{m,n,n_u} >> \lambda$, we can obtain the power of the received signal at the n_u UE from the $\mathcal{U}_{m,n}$ RIS unit cell as

$$P_{m,n,n_u} = \exp\left(-\kappa(f)\left(l_{m,n}^t + l_{m,n,n_u}\right)\right)$$
$$\times \frac{GU^r(\theta_i, \phi_i) P_{m,n}^r}{4\pi \left(l_{m,n,n_u}\right)^2} U^t(\theta_r, \phi_r) S_{n_u}^r, \tag{56}$$

where $S_{n_u}^r$ is the aperture of the n_u-th UE receive antenna and can be obtained as

$$S_{n_u}^r = \frac{G_{n_u}\lambda^2}{4\pi}. \tag{57}$$

With the aid of (57), (56) can be rewritten as

$$P_{m,n,n_u} = \frac{d_x d_y \lambda^2 U^r(\theta_i, \phi_i) U^t(\theta_r, \phi_r) G|R_{m,n}|^2 G_{AP} G_{n_u}}{(4\pi)^3 \left(l_{m,n,n_u}\right)^2 \left(l_{m,n}^t\right)^2}$$
$$\times \exp\left(-\kappa(f)\left(l_{m,n}^t + l_{m,n,n_u}\right)\right) P_{AP}. \tag{58}$$

As a result, the electrical field of the received signal at the n_u UE from the $\mathcal{U}_{m,n}$ RIS unit cell can be expressed as

$$E_{m,n,n_u} = \sqrt{2Z_o \frac{P_{m,n,n_u}}{S_{n_u}^r}} \exp\left(-j\frac{2\pi}{\lambda}\left(l_{m,n}^t + l_{m,n,n_u}\right)\right), \tag{59}$$

which, based on (58), can be equivalently written as

$$E_{m,n,n_u} = \frac{R_{m,n}\sqrt{2Z_o d_x d_y U^r(\theta_i, \phi_i) U^t(\theta_r, \phi_r) GG_{AP}P_{AP}}}{4\pi l_{m,n,n_u} l_{m,n}^t}$$
$$\times \exp\left(-\left(\frac{1}{2}\kappa(f) + j\frac{2\pi}{\lambda}\right)\left(l_{m,n}^t + l_{m,n,n_u}\right)\right). \tag{60}$$

Then, the total electric field at the n_u UE can be evaluated as

$$E_{n_u}^r = \sum_{m=-\frac{M}{2}+1}^{\frac{M}{2}} \sum_{n=-\frac{N}{2}+1}^{\frac{N}{2}} E_{m,n,n_u}, \tag{61}$$

which, by substituting (60) and taking into account that in the far-field $|R_{m,n}| \approx |R|$, can be equivalently expressed as in (62), as shown at the bottom of this page.

The AP position can be obtained as

$$\mathbf{r}_t = d_1 \sin(\theta_i) \cos(\phi_i) \mathbf{x}_o + d_1 \sin(\theta_i) \sin(\phi_i) \mathbf{y}_o$$
$$+ d_1 \cos(\theta_i) \mathbf{z}_o. \tag{63}$$

Thus, by employing (1) and (63), the distance between the AP and the $\mathcal{U}_{m,n}$ can be obtained as in (64),

$$l_{m,n}^t = \left(\left(d_1 \sin(\theta_i)\cos(\phi_i) - \left(n - \frac{1}{2}\right)d_x\right)^2 \right.$$
$$\left. + \left(d_1 \sin(\theta_i)\sin(\phi_i) - \left(m - \frac{1}{2}\right)d_y\right)^2 + d_1^2 \cos^2(\theta_i)\right)^{1/2} \tag{64}$$

By employing the Taylor expansion in (64) and keeping only the first term, the distance between the AP and the $\mathcal{U}_{m,n}$ can be approximated as

$$l_{m,n}^t \approx d_1 - \sin(\theta_i)\cos(\phi_i)\left(n - \frac{1}{2}\right)d_x$$
$$- \sin(\theta_i)\sin(\phi_i)\left(m - \frac{1}{2}\right)d_y \tag{65}$$

Following the same steps, we can prove that

$$l_{m,n,n_u} \approx d_{n_u} - \sin(\theta_r)\cos(\phi_r)\left(n - \frac{1}{2}\right)d_x$$
$$- \sin(\theta_r)\sin(\phi_r)\left(m - \frac{1}{2}\right)d_y. \tag{66}$$

By substituting (65) and (66) into (62), and taking into account that in practice d_x and d_y are at the order of $\lambda/10$, while $d_1, d_{nu} >> \lambda$, we can tightly approximate the electric field at the n_u UE as in (67), as shown at bottom of the next page. In (67),

$$\beta_{m,n} = d_1 - \sin(\theta_i)\cos(\theta_i)\left(n - \frac{1}{2}\right)d_x$$
$$- \sin(\theta_i)\sin(\theta_i)\left(m - \frac{1}{2}\right)d_y$$
$$+ d_{n_u} - \sin(\theta_r)\cos(\phi_r)\left(n - \frac{1}{2}\right)d_x$$
$$- \sin(\theta_r)\sin(\phi_r)\left(m - \frac{1}{2}\right)d_y. \tag{68}$$

The received signal power at the n_u UE can be evaluated as

$$P_r = \frac{|E_{n_u}^r|^2}{2Z_o} S_{n_u}^r, \tag{69}$$

$$E_{n_u}^r = \frac{|R|\sqrt{2Z_o d_x d_y U^r(\theta_i, \phi_i) U^t(\theta_r, \phi_r) GG_{AP}P_{AP}}}{4\pi} \sum_{m=-\frac{M}{2}+1}^{\frac{M}{2}} \sum_{n=-\frac{N}{2}+1}^{\frac{N}{2}} \frac{\exp\left(-\left(\frac{1}{2}\kappa(f) + j\frac{2\pi}{\lambda}\right)\left(l_{m,n}^t + l_{m,n,n_u}\right) + j\phi_{m,n}\right)}{l_{m,n,n_u} l_{m,n}^t} \tag{62}$$

which, with the aid of (57) and (67), can be written as

$$P_r = \frac{d_x d_y \lambda^2 |R|^2 U^r(\theta_t, \phi_t) U^t(\theta_r, \phi_r) GG_{AP}G_{n_u}P_{AP}}{64\pi^3 d_1^2 d_{n_u}^2}$$

$$\times \exp\left(-\kappa(f)\left(d_1 + d_{n_u}\right)\right) |\gamma|^2. \quad (70)$$

In (70), γ can be evaluated as in (71),

$$\gamma = \sum_{m=-\frac{M}{2}+1}^{\frac{M}{2}} \sum_{n=-\frac{N}{2}+1}^{\frac{N}{2}}$$

$$\times \exp\left(j\frac{2\pi}{\lambda}\left(d_1 + d_{n_u} - \beta_{m,n} + \frac{\lambda}{2\pi}\phi_{m,n}\right)\right) \quad (71)$$

or equivalently

$$\gamma = \gamma_1 \gamma_2, \quad (72)$$

where γ_1 and γ_2 respectively obtained as in (73) and (74),

$$\gamma_1 = \sum_{n=-\frac{N}{2}+1}^{\frac{N}{2}} \exp\left(j\frac{2\pi}{\lambda}\left(\sin(\theta_i)\cos(\theta_i)\left(n - \frac{1}{2}\right)d_x\right.\right.$$

$$\left.\left. + \sin(\theta_r)\cos(\phi_r)\left(n - \frac{1}{2}\right)d_x + \zeta_1\right)\right) \quad (73)$$

$$\gamma_2 = \sum_{m=-\frac{M}{2}+1}^{\frac{M}{2}} \exp\left(j\frac{2\pi}{\lambda}\left(\sin(\theta_i)\sin(\theta_i)\left(m - \frac{1}{2}\right)d_y\right.\right.$$

$$\left.\left. + \sin(\theta_r)\sin(\phi_r)\left(m - \frac{1}{2}\right)d_y + \zeta_2\right)\right) \quad (74)$$

In (73) and (74), ζ_1 and ζ_2 are defined in (4). By taking into account the sum of geometric progression theorem, (73) can be rewritten as

$$\gamma_1 = \frac{\exp\left(-j\frac{N\pi}{\lambda}\delta_1\right) - \exp\left(j\frac{N\pi}{\lambda}\delta_1\right)}{\exp\left(-j\frac{\pi}{\lambda}\delta_1\right) - \exp\left(j\frac{\pi}{\lambda}\delta_1\right)}, \quad (75)$$

or equivalently $\gamma_1 = \frac{\sin\left(\frac{N\pi}{\lambda}\delta_1\right)}{\sin\left(\frac{\pi}{\lambda}\delta_1\right)}$, or

$$\gamma_1 = N\frac{\text{sinc}\left(\frac{N\pi}{\lambda}\delta_1\right)}{\text{sinc}\left(\frac{\pi}{\lambda}\delta_1\right)}, \quad (76)$$

where

$$\delta_1 = (\sin(\theta_i)\cos(\theta_i) + \sin(\theta_r)\cos(\phi_r))d_x + \zeta_1. \quad (77)$$

By substituting (77) into (76), we get

$$\gamma_1 = N\frac{\text{sinc}\left(\frac{N\pi}{\lambda}(\sin(\theta_i)\cos(\phi_i) + \sin(\theta_r)\cos(\phi_r) + \zeta_1)d_x\right)}{\text{sinc}\left(\frac{\pi}{\lambda}(\sin(\theta_i)\cos(\phi_i) + \sin(\theta_r)\cos(\phi_r) + \zeta_1)d_x\right)}. \quad (78)$$

Similarly, (74) can be expressed as

$$\gamma_2 = M\frac{\text{sinc}\left(\frac{M\pi}{\lambda}(\sin(\theta_i)\sin(\phi_i) + \sin(\theta_r)\sin(\phi_r) + \zeta_2)d_y\right)}{\text{sinc}\left(\frac{\pi}{\lambda}(\sin(\theta_i)\sin(\phi_i) + \sin(\theta_r)\sin(\phi_r) + \zeta_2)d_y\right)}. \quad (79)$$

Finally, by substituting (78) and (79) into (72) and then to (70), we obtain (2). This concludes the proof.

B. PROOF OF THEOREM 2

Since θ_{n_u} is uniformly distributed with lower and upper bounds 0 and 2π, respectively, $\cos(\theta_{n_u})$ follows arc sine distribution with lower and upper bounds -1 and 1. Thus, the PDF of $\mathcal{D} = \cos(\theta_{n_u})$ can be expressed as

$$f_{\mathcal{D}}(y) = \begin{cases} \frac{1}{\pi\sqrt{1-y^2}}, & -1 < y < 1 \\ 0, & \text{otherwise} \end{cases}. \quad (80)$$

According to [70], since $\mathcal{D}$ and r_{n_u} are independent, the PDF of $\mathcal{Z}$ can be evaluated as

$$f_{\mathcal{Z}}(x) = \int_{|x|}^{r_e} f_{r_{n_u}}(r)f_{\mathcal{D}}\left(\frac{z}{r}\right)\frac{1}{r}\text{dr}. \quad (81)$$

By substituting (33) and (80) into (81), we can rewrite the PDF of $\mathcal{X}$ as

$$f_{\mathcal{Z}}(x) = \frac{2}{\pi r_e^2}\int_x^{r_e}\frac{r}{\sqrt{r^2 - x^2}}\text{dr}, \quad (82)$$

which, after performing the integration, can be expressed as (36).

The CDF of $\mathcal{X}$ can be evaluated as

$$F_{\mathcal{Z}}(x) = \int_{-r_e}^x f_{\mathcal{Z}}(y)\text{dy}, \quad (83)$$

which, with the aid of (36) and after some algebraic manipulations, can be rewritten as

$$F_{\mathcal{Z}}(x) = \frac{2}{\pi}\int_{-1}^{\frac{x}{r_e}}\sqrt{1 - u^2}\text{du}. \quad (84)$$

By employing [71], (84) can be written as (37). This concludes the proof.

$$E_{n_u}^r \approx \frac{|R|\sqrt{2Z_o d_x d_y U^r(\theta_i, \phi_i) U^t(\theta_r, \phi_r) GG_{AP}P_{AP}}}{4\pi d_1 d_{n_u}}$$

$$\times \exp\left(-\frac{1}{2}\kappa(f)\left(d_1 + d_{n_u}\right)\right)\sum_{m=-\frac{M}{2}+1}^{\frac{M}{2}}\sum_{n=-\frac{N}{2}+1}^{\frac{N}{2}}\exp\left(j\frac{2\pi}{\lambda}\left(d_1 + d_{n_u} - \beta_{m,n} + \frac{\lambda}{2\pi}\phi_{m,n}\right)\right) \quad (67)$$

C. PROOF OF THEOREM 3

From (32), we can obtain the CDF of d_{n_u} as

$$F_{d_{n_u}}(x) = \Pr\left(d_{n_u} \leq x\right), \tag{85}$$

or equivalently

$$F_{d_{n_u}}(x) = \Pr\left(\mathcal{Z} \geq d - x\right), \tag{86}$$

or

$$F_{d_{n_u}}(x) = 1 - F_{\mathcal{Z}}(d - x), \tag{87}$$

which, with the aid of (37), returns (38).

D. PROOF OF THEOREM 4

The CDF of the e2e channel coefficient is defined as

$$F_{h_{n_u}}(x) = \Pr\left(h_{n_u} \leq x\right), \tag{88}$$

which, based on (26), can be rewritten as

$$F_{h_{n_u}}(x) = \Pr\left(\mathcal{X} \leq \frac{x}{h_{n_u}^l}\right). \tag{89}$$

By employing (28), (89) can be expressed as

$$F_{h_{n_u}}(x) = \Pr\left(d_{n_u} \geq \frac{2h_{n_u}^l}{\kappa(f)\left(x + h_{n_u}^l\right)}\right), \tag{90}$$

or equivalently

$$F_{h_{n_u}}(x) = 1 - \Pr\left(d_{n_u} \leq \frac{2h_{n_u}^l}{\kappa(f)\left(x + h_{n_u}^l\right)}\right), \tag{91}$$

or

$$F_{h_{n_u}}(x) = 1 - F_{d_{n_u}}\left(\frac{2h_{n_u}^l}{\kappa(f)\left(x + h_{n_u}^l\right)}\right), \tag{92}$$

which, with the aid of (38), returns (39). This concludes the proof.

E. PROOF OF THEOREM 5

From (40), with the aid of (2) and (26), we can evaluate the coverage probability as

$$P_c = \Pr\left(h_{n_u} \leq \sqrt{\frac{P_{th}}{P_{AP}}}\middle| r_e = r_{th}\right), \tag{93}$$

or

$$P_c = F_{h_{n_u}}\left(\sqrt{\frac{P_{th}}{P_{AP}}}\middle| r_e = r_{th}\right), \tag{94}$$

which, by employing (39) gives (44). This concludes the proof.

REFERENCES

[1] F. Tariq, M. R. A. Khandaker, K.-K. Wong, M. A. Imran, M. Bennis, and M. Debbah, "A speculative study on 6G," *IEEE Wireless Commun.* vol. 27, no. 4, pp. 118–125, Aug. 2020, doi: 10.1109/MWC.001.1900488.

[2] A.-A. A. Boulogeorgos and G. K. Karagiannidis, "Low-cost cognitive radios against spectrum scarcity," *IEEE Tech. Committee Cogn. Netw. Newslett.*, vol. 3, no. 2, pp. 30–34, Nov. 2017.

[3] A.-A. A. Boulogeorgos, "Interference mitigation techniques in modern wireless communication systems," Ph.D. dissertation, Aristotle Univ. Thessaloniki, Thessaloniki, Greece, Sep. 2016.

[4] C. Zhang, K. Ota, J. Jia, and M. Dong, "Breaking the blockage for big data transmission: Gigabit road communication in autonomous vehicles," *IEEE Commun. Mag.*, vol. 56, no. 6, pp. 152–157, Jun. 2018.

[5] S. Dang, O. Amin, B. Shihada, and M.-S. Alouini, "What should 6G be?," *Nat. Electron.*, vol. 3, no. 1, pp. 20–29, Jan. 2020.

[6] L. Bariah *et al.*, "Prospective look: Key enabling technologies, applications and open research topics in 6G networks," 2020, *ArXiv:2004.06049*.

[7] I. F. Akyildiz, J. M. Jornet, and C. Han, "Terahertz band: Next frontier for wireless communications," *Phys. Commun.*, vol. 12, pp. 16–32, Sep. 2014.

[8] Z. Xu, X. Dong, and J. Bornemann, "Design of a reconfigurable mimo system for thz communications based on graphene antennas," *IEEE Trans. THz Sci. Technol.*, vol. 4, no. 5, pp. 609–617, Sep. 2014.

[9] R. Zhang, K. Yang, Q. H. Abbasi, K. A. Qaraqe, and A. Alomainy, "Analytical characterisation of the terahertz in-vivo nano-network in the presence of interference based on TS-OOK communication scheme," *IEEE Access*, vol. 5, pp. 10 172–10 181, Jun. 2017.

[10] A.-A. A. Boulogeorgos *et al.*, "Terahertz technologies to deliver optical network quality of experience in wireless systems beyond 5G," *IEEE Commun. Mag.*, vol. 56, no. 6, pp. 144–151, Jun. 2018.

[11] T. S. Rappaport *et al.*, "Wireless communications and applications above 100 GHz: Opportunities and challenges for 6G and beyond," *IEEE Access*, vol. 7, pp. 78 729–78 757, Jun. 2019.

[12] A.-A. A. Boulogeorgos *et al.*, "Wireless terahertz system architectures for networks beyond 5G," 2018, *ArXiv:1810.12260*.

[13] C. Lin and G. Y. L. Li, "Terahertz communications: An array-of-subarrays solution," *IEEE Commun. Mag.*, vol. 54, no. 12, pp. 124–131, Dec. 2016.

[14] A. Leuther, T. Merkle, R. Weber, R. Sommer, and A. Tessmann, "THz frequency HEMTs: Future trends and applications," in *Proc. Compound Semicond. Week (CSW)*, Nara, Japan, May 2019, pp. 1–2.

[15] A. C. Tasolamprou *et al.*, "Exploration of intercell wireless millimeter-wave communication in the landscape of intelligent metasurfaces," *IEEE Access*, vol. 7, pp. 122 931–122948, Aug. 2019.

[16] Q. Wu and R. Zhang, "Intelligent reflecting surface enhanced wireless network: Joint active and passive beamforming design," in *Proc. IEEE Global Commun. Conf.*, Dec. 2018, pp. 1–6.

[17] Q. Wu and R. Zhang, "Beamforming optimization for intelligent reflecting surface with discrete phase shifts," in *Proc. IEEE Int. Conf. Acoust., Speech Signal Process.*, May 2019, pp. 7830–7833.

[18] E. Basar, M. Di Renzo, J. De Rosny, M. Debbah, M. Alouini, and R. Zhang, "Wireless communications through reconfigurable intelligent surfaces," *IEEE Access*, vol. 7, pp. 116 753–116773, 2019.

[19] M. D. Renzo *et al.*, "Smart radio environments empowered by reconfigurable ai meta-surfaces: An idea whose time has come," *EURASIP J. Wireless Commun. Netw.*, vol. 2019, no. 1, pp. 1–20, May 2019.

[20] S. V. Hum and J. Perruisseau-Carrier, "Reconfigurable reflectarrays and array lenses for dynamic antenna beam control: A review," *IEEE Trans. Antennas Propag.*, vol. 62, no. 1, pp. 183–198, Jan. 2014.

[21] J. M. Jornet and I. F. Akyildiz, "Channel modeling and capacity analysis for electromagnetic wireless nanonetworks in the terahertz band," *IEEE Trans. Wireless Commun.*, vol. 10, no. 10, pp. 3211–3221, Oct. 2011.

[22] P. Boronin, V. Petrov, D. Moltchanov, Y. Koucheryavy, and J. M. Jornet, "Capacity and throughput analysis of nanoscale machine communication through transparency windows in the terahertz band," *Nano Commun. Netw.*, vol. 5, no. 3, pp. 72–82, Sep. 2014.

[23] K. Yang, A. Pellegrini, M. O. Munoz, A. Brizzi, A. Alomainy, and Y. Hao, "Numerical analysis and characterization of THz propagation channel for body-centric nano-communications," *IEEE Trans. THz Sci. Technol.*, vol. 5, no. 3, pp. 419–426, May 2015.

[24] C. Han, A. O. Bicen, and I. F. Akyildiz, "Multi-ray channel modeling and wideband characterization for wireless communications in the terahertz band," *IEEE Trans. Wireless Commun.*, vol. 14, no. 5, pp. 2402–2412, May 2015.

[25] J. Kokkoniemi, J. Lehtomäki, and M. Juntti, "Simplified molecular absorption loss model for 275-400 gigahertz frequency band," in *Proc. 12th Eur. Conf. Antennas Propag.*, London, U.K., Apr. 2018, pp. 1–5.

[26] E. N. Papasotiriou, J. Kokkoniemi, A.-A. A. Boulogeorgos, J. Lehtomäki, A. Alexiou, and M. Juntti, "A new look to 275 to 400 ghz band: Channel model and performance evaluation," in *Proc. IEEE Int. Symp. Pers., Indoor Mobile Radio Commun.*, Bolonia, Italy, Sep. 2018, pp. 1–5.

[27] A.-A. A. Boulogeorgos, E. N. Papasotiriou, J. Kokkoniemi, J. Lehtomäki, A. Alexiou, and M. Juntti, "Performance evaluation of THz wireless systems operating in 275-400 GHz band," in *Proc. IEEE Veh. Technol. Conf.*, 2018, pp. 1–5.

[28] A. Afsharinejad, A. Davy, B. Jennings, and C. Brennan, "An initial path-loss model within vegetation in the thz band," in *Proc. 9th Eur. Conf. Antennas Propag.*, May 2015, pp. 1–5.

[29] A.-A. A. Boulogeorgos, E. N. Papasotiriou, and A. Alexiou, "Analytical performance assessment of THz wireless systems," *IEEE Access*, vol. 7, pp. 11436–11453, 2019.

[30] A.-A. A. Boulogeorgos and A. Alexiou, "Error analysis of mixed THz-RF wireless systems," *IEEE Commun. Lett.*, vol. 24, no. 2, pp. 277–281, Feb. 2020.

[31] A.-A. A. Boulogeorgos, E. N. Papasotiriou, and A. Alexiou, "A distance and bandwidth dependent adaptive modulation scheme for THz communications," in *Proc. 19th IEEE Int. Workshop Signal Process. Adv. Wireless Commun.*, Jul. 2018, pp. 1–5.

[32] A.-A. A. Boulogeorgos, S. Goudos, and A. Alexiou, "Users association in ultra dense THz networks," in *Proc. IEEE Int. Workshop Signal Process. Adv. Wireless Commun.*, Jun. 2018, pp. 1–5.

[33] A.-A. A. Boulogeorgos and A. Alexiou, "Performance evaluation of the initial access procedure in wireless THz systems," in *Proc. IEEE 16th Int. Symp. Wireless Commun. Syst.*, Aug. 2019, pp. 422–426.

[34] A. Afsharinejad, A. Davy, B. Jennings, S. Rasmann, and C. Brennan, "A path-loss model incorporating shadowing for THz band propagation in vegetation," in *Proc. IEEE Global Commun. Conf.*, Dec. 2015, pp. 1–6.

[35] H. Elayan, R. M. Shubair, J. M. Jornet, and P. Johari, "Terahertz channel model and link budget analysis for intrabody nanoscale communication," *IEEE Trans. Nanobiosci.*, vol. 16, no. 6, pp. 491–503, Sep. 2017.

[36] M. A. Akkas, "Terahertz channel modelling of wireless ultra-compact sensor networks using electromagnetic waves," *IET Commun.*, vol. 10, no. 13, pp. 1665–1672, 2016.

[37] A.-A. A. Boulogeorgos and A. Alexiou, "Antenna misalignment and blockage in THz communications," in *Next Generation Wireless Terahertz Communication Networks*, Boca Raton, FL, USA: CRC Press, 2020.

[38] T. Merkle *et al.*, "Testbed for phased array communications from 275 to 325 GHz," in *Proc. IEEE Compound Semicond. Integr. Circuit Symp.*, Oct. 2017, pp. 1–4.

[39] O. Erturk and T. Yilmaz, "A hexagonal grid based human blockage model for the 5 G low terahertz band communications," in *Proc. IEEE 5G World Forum (5GWF)*, Jul. 2018, pp. 395–398.

[40] A. Shafie, N. Yang, Z. Sun, and S. Durrani, "Coverage analysis for 3d terahertz communication systems with blockage and directional antennas," in *Proc. IEEE Int. Conf. Commun. Workshops.*, Jun. 2020, pp. 1–7.

[41] Y. Wu, J. Kokkoniemi, C. Han, and M. Juntti, "Interference and coverage analysis for terahertz networks with indoor blockage effects and line-of-sight access point association," *IEEE Trans. Wireless Commun.*, to be published.

[42] M. Jung, W. Saad, Y. R. Jang, G. Kong, and S. Choi, "Performance analysis of large intelligence surfaces (LISs): Asymptotic data rate and channel hardening effects," Arxiv, 2018. [Online]. Available: http://arxiv.org/abs/1810.05667

[43] C. Huang, A. Zappone, G. C. Alexandropoulos, M. Debbah, and C. Yuen, "Reconfigurable intelligent surfaces for energy efficiency in wireless communication," *IEEE Trans. Wireless Commun.*, vol. 18, no. 8, pp. 4157–4170, Aug. 2019.

[44] V. C. Thirumavalavan and T. S. Jayaraman, "BER analysis of reconfigurable intelligent surface assisted downlink power domain NOMA system," in *Proc. Int. Conf. Commun. Syst. Netw.*, Bengaluru, India, Jan. 2020, pp. 519–522.

[45] M. D. Renzo *et al.*, "Reconfigurable intelligent surfaces vs. relaying: Differences, similarities, and performance comparison," *IEEE Open J. Commun. Soc.*, vol. 1, pp. 798–807, 2020.

[46] E. Bjornson, O. Ozdogan, and E. G. Larsson, "Intelligent reflecting surface versus decode-and-forward: How large surfaces are needed to beat relaying?" *IEEE Wireless Commun. Lett.*, vol. 9, no. 2, pp. 244–248, Feb. 2020.

[47] A.-A. A. Boulogeorgos and A. Alexiou, "Performance analysis of reconfigurable intelligent surface-assisted wireless systems and comparison with relaying," *IEEE Access*, vol. 8, pp. 94 463–94483, May 2020.

[48] A.-A. A. Boulogeorgos and A. Alexiou, "How much do hardware imperfections affect the performance of reconfigurable intelligent surface-assisted systems?," *IEEE Open J. Commun. Soc.*, vol. 1, pp. 1185–1195, Aug. 2020.

[49] X. Ma *et al.*, "Joint channel estimation and data rate maximization for intelligent reflecting surface assisted terahertz MIMO communication systems," *IEEE Access*, vol. 8, pp. 99 565–99581, May 2020.

[50] J. Qiao and M.-S. Alouini, "Secure transmission for intelligent reflecting surface-assisted mmWave and terahertz systems," *IEEE Wireless Commun. Lett.*, vol. 9, no. 10, pp. 1743–1747, Oct. 2020.

[51] K. Tekbyk, G. K. Kurt, A. R. Ekti, A. Grin, and H. Yanikomeroglu, "Reconfigurable intelligent surface empowered terahertz communication for leo satellite networks," Jul. 2020, Arxiv.

[52] S. P. Maruthi, T. Panigrahi, and M. Hassan, "Improving the reliability of pulse-based terahertz communication using intelligent reflective surface," in *Proc. IEEE Int. Conf. Commun. Workshops.*, Jun. 2020, pp. 1–6.

[53] E. N. Papasotiriou, J. Kokkoniemi, A.-A. A. Boulogeorgos, J. Lehtomäki, A. Alexiou, and M. Juntti, "A new look to 275 to 400 GHz band: Channel model and performance evaluation," in *Proc. IEEE Int. Symp. Pers., Indoor Mobile Radio Commun.*, Bolonia, Italy, Sep. 2018, pp. 1–5.

[54] J. Kokkoniemi, J. Lehtomäki, and M. Juntti, "A line-of-sight channel model for the 100-450 gigahertz frequency band," Feb. 2020, arXiv.

[55] S. W. Ellingson, "Path loss in reconfigurable intelligent surface-enabled channels," Dec. 2019, Arxiv,"

[56] W. Tang *et al.*, "Wireless communications with reconfigurable intelligent surface: Path loss modeling and experimental measurement," Nov. 2019, Arxiv,"

[57] R. Goody and Y. Yung, *Atmospheric Radiation: Theoretical Basis*. New York, NY, USA: Oxford Univ. Press, 1995.

[58] L. S. Rothman *et al.*, "The HITRAN 2008 molecular spectroscopic database," *J. Quant. Spectrosc. Radiat. Transfer*, vol. 110, no. 9, pp. 533–572, Jun. 2009.

[59] D. Zwillinger, *Standard Mathematical Tables and Formulae*. London, U.K.: Chapman & Hall/CRC, 2003.

[60] S. Koenig *et al.*, "Wireless sub-THz communication system with high data rate," *Nat. Photon.*, vol. 7, Oct. 2013.

[61] T. Nagatsuma, G. Ducournau, and C. C. Renaud, "Advances in terahertz communications accelerated by photonics," *Nat. Photon.*, vol. 10, May 2016.

[62] C. A. Balanis, *Modern Antenna Handbook*. Hoboken, NJ, USA: Wiley-Interscience, 2008.

[63] W. Stutzman, *Antenna Theory and Design*. Hoboken, NJ, USA: Wiley, 2013.

[64] V. S. Asadchy, M. Albooyeh, S. N. Tcvetkova, A. Diaz-Rubio, Y. Radi, and S. A. Tretyakov, "Perfect control of reflection and refraction using spatially dispersive metasurfaces," *Phys. Rev. B*, vol. 94, no. 7, Aug. 2016.

[65] R. Xu, H. Zhu, and J. Yuan, "Electric-field intrabody communication channel modeling with finite-element method," *IEEE Trans. Biomed. Eng.*, vol. 58, no. 3, pp. 705–712, Mar. 2011.

[66] R. Xu, W. C. Ng, H. Zhu, H. Shan, and J. Yuan, "Equation environment coupling and interference on the electric-field intrabody communication channel," *IEEE Trans. Biomed. Eng.*, vol. 59, no. 7, pp. 2051–2059, Jul. 2012.

[67] A. Shafie, N. Yang, and C. Han, "Multi-connectivity for indoor terahertz communication with self and dynamic blockage," in *Proc. IEEE Int. Conf. Commun.*, Dublin, Ireland, Jun. 2020, pp. 1–7.

[68] Z. Hossain and J. M. Jornet, "Hierarchical bandwidth modulation for ultra-broadband terahertz communications," in *IEEE Proc. Int. Conf. Commun.*, May 2019, pp. 1–7.

[69] C. Han and I. F. Akyildiz, "Distance-aware bandwidth-adaptive resource allocation for wireless systems in the terahertz band," *IEEE Trans. THz Sci. Technol.*, vol. 6, no. 4, pp. 541–553, Jul. 2016.

[70] J. J. Shynk, *Probability, Random Variables, and Random Processes: Theory and Signal Processing Applications*. Hoboken, NJ, USA: Wiley, 2013.

[71] I. S. Gradshteyn and I. M. Ryzhik, *Table of Integrals, Series, and Products*, 6th ed. San Francisco, CA, USA: Academic, 2000.

ALEXANDROS-APOSTOLOS A. BOULOGEOR-GOS (Senior Member, IEEE) was born in Trikala, Greece, in 1988. He received the Electrical and Computer Engineering (ECE) diploma and the Ph.D. degree in wireless communications from the Aristotle University of Thessaloniki (AUTh), Thessaloniki, Greece, in 2012 and 2016, respectively.

Since November 2012, he has been a Member of the Wireless Communications System Group with AUTh and a Research Assistant or Project Engineer in various national and European communication and networks projects. During 2017, he joined the Information Technologies Institute (ITI), Centre for Research & Technology Hellas (CERTH), Marousi, Greece, and in November 2017, he joined the Department of Digital Systems, University of Piraeus, Piraeus, Greece, where he conducts research in the area of wireless communications. From October 2012 to September 2016, he was a Teaching Assistant with the Department of ECE, AUTh, and in February 2017, he was an Adjunct Professor with the Department of ECE, University of Western Macedonia, Kozani, Greece, and a Visiting Lecturer with the Department of Computer Science and Biomedical Informatics, University of Thessaly, Volos, Greece.

He has authored and coauthored more than 60 technical papers, which were published in scientific journals and presented at prestigious international conferences, and holds two, one national and one European, patents. His current research interests include wireless communications and networks with emphasis in high-frequency communications, optical wireless communications, and communications and digital signal processing for biomedical applications. He has been a Member of Technical Program Committees in several IEEE and non-IEEE conferences, and was a Reviewer in various IEEE journals and conferences. He was the recipient of the Distinction Scholarship Award of the Research Committee of AUTh in 2014, and was recognized as an Exemplary Reviewer for the IEEE COMMUNICATION LETTERS in 2016 (top 3% of reviewers) and a Top Peer Reviewer (top 1% of reviewers) in cross-field and computer science in the Global Peer Review Awards 2019, which was presented by the *Web of Science* and *Publons*. He is a Member of the Technical Chamber of Greece. He is currently the Editor of the IEEE COMMUNICATIONS LETTERS and an Associate Editor for the *Frontier In Communications And Networks*.

ANGELIKI ALEXIOU (Member, IEEE) received the diploma in electrical and computer engineering from the National Technical University of Athens, Athens, Greece, in 1994 and the Ph.D. degree in electrical engineering from the Imperial College of Science, Technology and Medicine, University of London, London, U.K., in 2000. She is currently a Professor with the Department of Digital Systems, ICT School, University of Piraeus, Piraeus, Greece. Since May 2009, she has been a Faculty Member with the Department of Digital Systems, where she conducts research and teaches undergraduate and postgraduate courses in the area of broadband communications and advanced wireless technologies. Prior to this appointment, she was with Bell Laboratories, Wireless Research, Lucent Technologies (later Alcatel-Lucent, now NOKIA), Swindon, U.K., first as a Member of Technical Staff from January 1999 to February 2006 and later as a Technical Manager from March 2006 to April 2009. Her current research interests include radio interface for 5G systems and beyond, MIMO and high frequencies (mmWave and THz wireless) technologies, cooperation, coordination, and efficient resource management for ultra dense wireless networks and machine-to-machine communications, cell-less architectures based on virtualization and extreme resources sharing, and machine learning for wireless systems. She was the corecipient of the Bell Labs President's Gold Award in 2002 for contributions to Bell Labs Layered Space-Time (BLAST) project and the Central Bell Labs Teamwork Award in 2004 for role model teamwork and technical achievements in the IST FITNESS project. She is the Chair of the Working Group on Radio Communication Technologies and of the Working Group on High Frequencies Radio Technologies of the Wireless World Research Forum. She is a Member of the Technical Chamber of Greece. She is the Project Coordinator of the H2020 TERRANOVA project (ict-terranova.eu) and the Technical Manager of the H2020 ARIADNE project.